



# The eVe reference polarisation lidar system for Cal/Val of Aeolus L2A product

Peristera Paschou<sup>1,2</sup>, Nikolaos Siomos<sup>1,2</sup>, Alexandra Tsekeri<sup>1</sup>, Alexandros Louridas<sup>3</sup>, George Georgoussis<sup>3</sup>, Volker Freudenthaler<sup>4</sup>, Ioannis Biniotoglou<sup>1,3</sup>, George Tsaknakis<sup>3</sup>, Alexandros Tavernarakis<sup>3</sup>, Christos Evangelatos<sup>3</sup>, Jonas von Bismarck<sup>5</sup>, Thomas Kanitz<sup>6</sup>, Charikleia Meleti<sup>2</sup>, Eleni Marinou<sup>1,2</sup> and Vassilis Amiridis<sup>1</sup>

<sup>1</sup> IAASARS, National Observatory of Athens, Athens, Greece

<sup>2</sup> Laboratory of Atmospheric Physics, Physics Department, Aristotle University of Thessaloniki, Thessaloniki, Greece

<sup>3</sup> Raymetrics S.A., Athens, Greece

10 <sup>4</sup> Fakultät für Physik, Meteorologisches Institut, Ludwig-Maximilians-Universität, Munich, Germany

<sup>5</sup> European Space Agency (ESA-ESRIN), Frascati, Italy

<sup>6</sup> European Space Agency (ESA-ESTEC), Noordwijk, The Netherlands

Correspondence to: Peristera Paschou ([pepaschou@noa.gr](mailto:pepaschou@noa.gr))

## Abstract.

15 The eVe dual-laser/dual-telescope lidar system is briefly given here, focusing on the optical and mechanical parts of system's emission and receiver units. The compact design of linear/circular emission unit along with the linear/circular analyser in the receiver unit, allows eVe to simultaneously reproduce the operation of the ALADIN lidar on board Aeolus as well as the operation of a traditional ground-based polarisation lidar system with linear emission. As such, eVe lidar aims to provide: (a) ground reference measurements for the validation of the Aeolus L2A aerosol products, and (b) the atmospheric conditions for  
20 which linear polarisation lidar systems can be considered for Aeolus L2A validation, by identifying any possible biases arisen from the different polarisation state in the emission between ALADIN and these systems, and the detection of only the co-polar component of the returned signal from ALADIN for the L2A products retrieval. In addition, a brief description is given concerning the polarisation calibration techniques that are applied in the system, as well as the developed software for the analysis of the collected signals and the retrieval of the optical products. More specifically, the system's dual configuration  
25 enables the retrieval of the optical properties of particle backscatter and extinction coefficients originating from the two different polarisation states of the emission, the linear and circular depolarisation ratios, as well as the direct calculation of the Aeolus like backscatter coefficient, i.e., the backscatter coefficient that Aeolus would measure from ground. Two cases, one with slightly-depolarising particles and one with moderately-depolarising particles, were selected from the first conducted measurements of eVe in Athens, in order to give a glimpse of the system's capabilities. In the slightly depolarising scene, the  
30 Aeolus like backscatter coefficient agrees well with the actual backscatter coefficient, which is also true when non-depolarising particles are present. The agreement however fades out for strongly depolarising scenes, where an underestimation of ~17 % of the Aeolus like backscatter coefficient is observed when moderately-depolarising particles are probed.



## 1. Introduction

The Calibration and Validation (Cal/Val) of spaceborne instruments for Earth Observation (EO) have traditionally relied on ground-based measurements provided by well-characterised reference systems (Holben et al., 1998; Pappalardo et al., 2014). The Aeolus mission (Reitebuch, 2012; Stoffelen et al., 2005), an atmospheric Earth Explorers Core mission of European Space Agency (ESA), is not an exception, particularly with respect to the Cal/Val of the wind, aerosol, and cloud product from the Atmospheric Laser Doppler Instrument (ALADIN). Aeolus is designed to provide global profiles of the Horizontal Line-of-Sight (HLOS) wind component in the troposphere and the lower stratosphere (Dabas, 2010; Stoffelen et al., 2006; Tan et al., 2008) through ALADIN, a sophisticated Doppler Wind Lidar (DWL; Paffrath et al., 2009; Reitebuch et al., 2009) and the only instrument onboard the platform. ALADIN is a High Spectral Resolution Lidar (HSRL) operating in the ultraviolet region of the spectrum at 355 nm wavelength, implemented in a transceiver configuration and tilted 35° from nadir (Lolli et al., 2013). The instrument utilizes a circularly polarised emission and a multiple-interferometer receiver for the detection of the backscattered light from molecules and particulates (i.e. aerosols and clouds) to the Rayleigh and Mie channels, respectively (Flamant et al., 2007). The Rayleigh and Mie signals are distinguished by considering the broader and the narrower scattered spectra for molecules and particulates, respectively, attributed to the Doppler effect (Imaki et al., 2005; Shipley et al., 1983). Besides the wind profiles, ALADIN is also capable of deriving particle optical properties such as the particle backscatter coefficient, the particle extinction coefficient, and the backscatter-to-extinction ratio (BER) (Ansmann et al., 2007; Flamant et al., 2008). However, ALADIN's configuration enables the detection of only the co-polar component of the backscattered circularly polarised emission resulting in the retrieval of the co-polar backscatter coefficient (see Appendix A). The missing cross-polar component is not negligible in case of depolarising particles in the atmosphere, such as ice crystals (e.g. Mishchenko and Sassen, 1998), dust (e.g. Freudenthaler et al., 2009), pollen (e.g. Sassen, 2008), and volcanic ash (e.g. Ansmann et al., 2010) or stratospheric smoke (e.g. Gialitaki et al., 2020). For non-depolarising particles, the co-polar backscatter coefficient can be calculated from the theory considering the depolarisation of the molecules (see Appendix A) and can approximate well the total backscatter coefficient, an extensive aerosol optical property that is commonly measured from the lidar systems (Ansmann et al., 1992; Fernald, 1984; Klett, 1981; Sasano and Nakane, 1984). This is not the case, in the presence of depolarising particles, where the co-polar backscatter coefficient is significantly smaller with respect to the total backscatter coefficient. In such cases, related discrepancies of up to 75 % for ice crystals and up to 50 % for dust or ash particles can be expected for the co-polar backscatter coefficient with respect to the total backscatter coefficient (Flamant et al., 2007), and the Aeolus L2A products of the particle backscatter coefficient and the BER will be underestimated. The Cal/Val of the Aeolus L2A products is, thus, far more suitable with lidar systems with polarisation capabilities, to identify ALADIN's inherent uncertainty for depolarising scenes. Such lidar systems have become increasingly popular within the aerosol remote sensing community (for instance, the European Aerosol Research Lidar Network – EARLINET, currently deploys 18 stations that perform lidar polarisation measurements; Pappalardo et al., 2004). The EARLINET systems apply linear depolarisation techniques.



In principle, the emitted linearly polarised light is backscattered mainly with the same linear polarisation and partly depolarised, upon interaction with atmospheric targets which are non-spherical and randomly oriented (Mishchenko and Hovenier, 1995). The polarisation sensitive detection of the collected backscattered signal is usually performed by separating the signal in two optical paths; the first (parallel or co-polar) contains the backscattered light with the original polarisation and half of the depolarised light, and the second (cross or cross-polar) contains the other half of the depolarised light (Gimmetad, 2008). There are also systems that rely on the detection of the total and cross backscattered signals instead (Engelmann et al., 2016). In both cases, profiles of the aerosol volume linear depolarisation ratio can be calculated from the two signals.

For atmospheric layers containing randomly oriented particles and where multiple scattering is negligible, the lidar measurements of the linear depolarisation ratio are sufficient for validating the Aeolus circular polarisation products, since the relationship between the linear and circular depolarisation ratios is known from theory (Mishchenko and Hovenier, 1995; Roy and Roy, 2008). Hence, the linear polarisation products can be easily converted to circular polarisation products (see Appendix A), facilitating the validation of Aeolus L2A products in an indirect way. On the other hand, for depolarising scenes where the aforementioned assumptions are not valid due to particle orientation (e.g. of desert dust; Daskalopoulou et al., 2021; Mallios et al., 2021; Ulanowski et al., 2007; and cirrus clouds e.g. Myagkov et al., 2016; Noel and Sassen, 2005; Thomas et al., 1990) and/or multiple scattering effects inside the clouds (Donovan et al., 2015; Jimenez et al., 2020a; Schmidt et al., 2013) and even within optically thick aerosol layers (Wandinger et al., 2010), the linear to circular polarisation products conversion is not applicable and a direct validation of the Aeolus L2A products is needed, using a polarisation lidar system with circularly polarised emission as ALADIN.

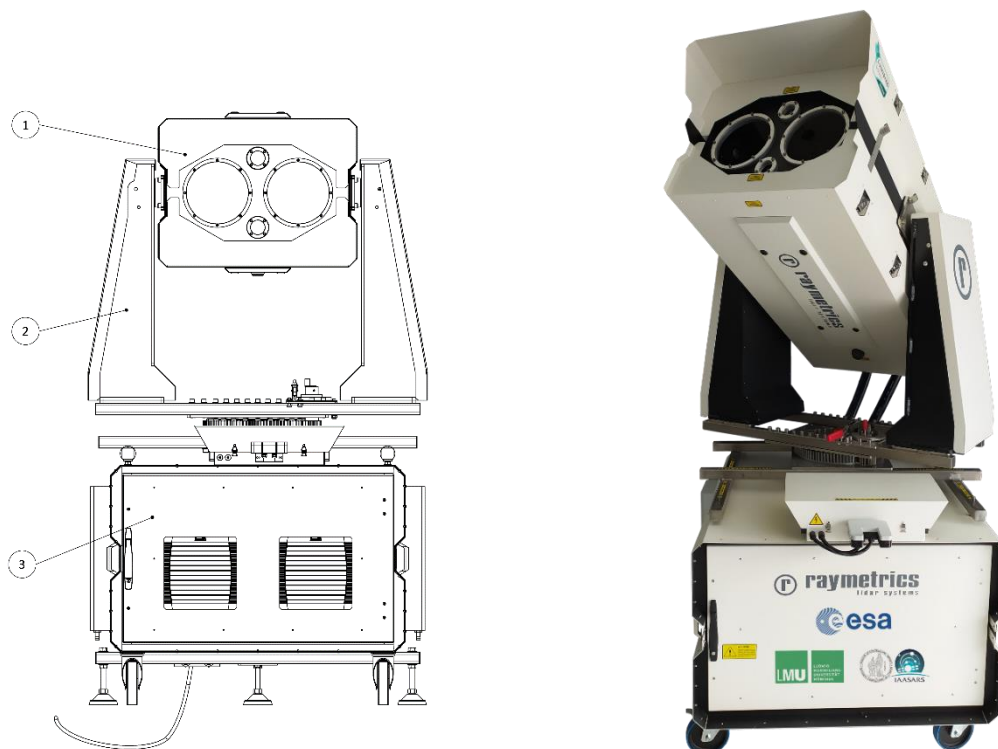
In this paper we present the eVe lidar system (Enhancement and Validation of Aeolus products), a combined linear/circular polarisation system designed to provide the Aeolus mission with ground-based reference measurements, facilitating the Aeolus L2A product validation, assessment, and optimisation. The system's design incorporates the necessary hardware elements to reproduce both the operation of ALADIN, that relies on circularly polarised emission, and the operation of a traditional polarisation lidar system with linearly polarised emission. Besides its main goal (i.e., to validate Aeolus L2A), the dual linear/circular configuration enables the examination of the conversion factors from linear to circular polarisation products for a wide variety of aerosol/cloud types. This procedure will consequently provide an evaluation of possible biases in Cal/Val studies performed with linear polarisation lidar systems (which are available worldwide). In addition, the eVe lidar can be used as the ground reference system for the validation of future ESA missions like EarthCARE (Illingworth et al., 2015).

Section 2 provides a brief description of the system, focusing on the mechanical and optical parts. Section 3 presents the polarisation calibration techniques that have been developed for EVE. The lidar signal processing and the optical products retrieval algorithm are described in Section 4. Section 5 presents the first optical products of eVe for two selected cases measured over Athens. The conversion formulas from the linear to circular polarisation products and vice versa, are given in Appendix A. Finally, we summarise and conclude in Section 6.



## 2. System overview

The eVe lidar has been constructed by Raymetrics S.A., Athens, Greece, in collaboration with the National Observatory of Athens and the Ludwig-Maximilians-Universität, Munich, Germany. The system has been designed to be a flexible and mobile ground-based lidar system, capable of operating under a wide range of ambient conditions. The system utilizes two lasers emitting linearly and circularly polarised light, respectively, and two telescopes, each collecting the backscattered light from both lasers. The collected backscattered signals are recorded by five photomultiplier tubes (PMT) in combined analogue and photon-counting mode (Licel GmbH, 2020). The three main components of the system are the lidar head, the positioner, and the electronics enclosure, as shown in Fig. 1. The lidar head is mounted on the positioner and both of them are mounted on the electronics enclosure. Moreover, the electronics enclosure and the lidar are connected with two umbilical tubes that contain the lasers' cooling lines as well as the power and communication cables; they have independent cooling/heating systems allowing the system to operate in ambient temperatures from 5° C up to 45° C. The system is also rain and dust proof with an IP rating of 55.



110 **Figure 1: The lidar head (1), the alt-azimuth positioner (2) and the electronic enclosure (3) of eVe lidar system**



## 2.1. The Lidar Head

The lidar head consists of the emission unit and the receiver unit, for which a detailed schematic of the head's internal parts is presented in Fig. 2. The internal components of the lidar head are protected from the ambient atmospheric conditions by the head metal covers, two laser windows, and two telescope windows. The head covers can be easily and fully removed, providing a full access to the internal parts for maintenance and troubleshooting purposes. Three thermoelectric coolers are also installed, to stabilize the internal temperature of the lidar head in  $30 \pm 2.5$  °C.

### 2.1.1. Emission

The emission unit contains two CFR400 model Nd:Yag lasers (LA and LB) manufactured by Lumibird S.A., both originally emitting linearly polarised laser pulses at 355 and 532 nm, and elliptically polarised pulses at 1064 nm due to the housed harmonic generation module inside the lasers. According to the laser manufacturer, the laser pulses are emitted with a repetition rate of 20 Hz and energies of ~89 and ~100 mJ at 355 nm, ~88 and ~97 mJ at 532 nm, and ~117 and ~135 mJ at 1064 nm for LA and LB, respectively, before the emission optics. LB is equipped with one motorised rotated quarter wave plate (QWP) placed at 45° with respect to the original laser polarisation orientation, for converting the linear polarisation to circular only for the laser pulses at 355 nm. Thus, LA emits a linearly polarised beam at the three wavelengths, while, the LB emits circularly polarised beam at 355 nm and elliptically polarised beam at 532 and 1064 nm.

### 2.1.2. Detection

Each receiver unit consists of an afocal system composed by a telescope (T1, T2) and a collimating lens (C1, C2), and a proximate wavelength separation unit (WSU) (see Fig. 2). The lasers and the telescopes are placed in a compact diamond-shaped layout ensuring equal distances for both lasers to both telescopes and also facilitating the alignment of both lasers with each telescope at the same time. The two telescopes are Dall-Kirkham type, utilizing an elliptical prolate primary mirror and a spherical secondary mirror, with an aperture of 200 mm and focal length of 1000 mm (F#5). One field stop in each receiver (FS1, FS2) is used for determining the field of view (FOV) of each receiver. The field stops are graduated ring-actuated iris diaphragms with minimum apertures of 1 mm and maximum of 12 mm. Currently, the iris diameters are set to 2 mm, resulting to a FOV of 2 mrad, achieving good sky background light suppression while achieving a full overlap range at 400 m. Each WSU is mounted to its telescope on a manual rotator (M) that can rotate the whole WSU around the optical axis with a fixed step of 45°, and continuously in a small range around the zero position in order to compensate for a mechanical misalignment with respect to the laser polarisation orientation. The manual rotator is used for calibration purposes (Section 3). Motorised shutters (LMC1:P1 and LMC2:P1) are placed behind the manual rotator in both WSUs to block the entrance of light in the WSU, facilitating the dark signal measurements. In WSU1, the incoming collimated light passes through a dichroic long pass mirror (DM1), transmitting wavelengths larger than the 365 nm and reflecting all smaller wavelengths. The transmitted light goes through an interference filter (IFF) with

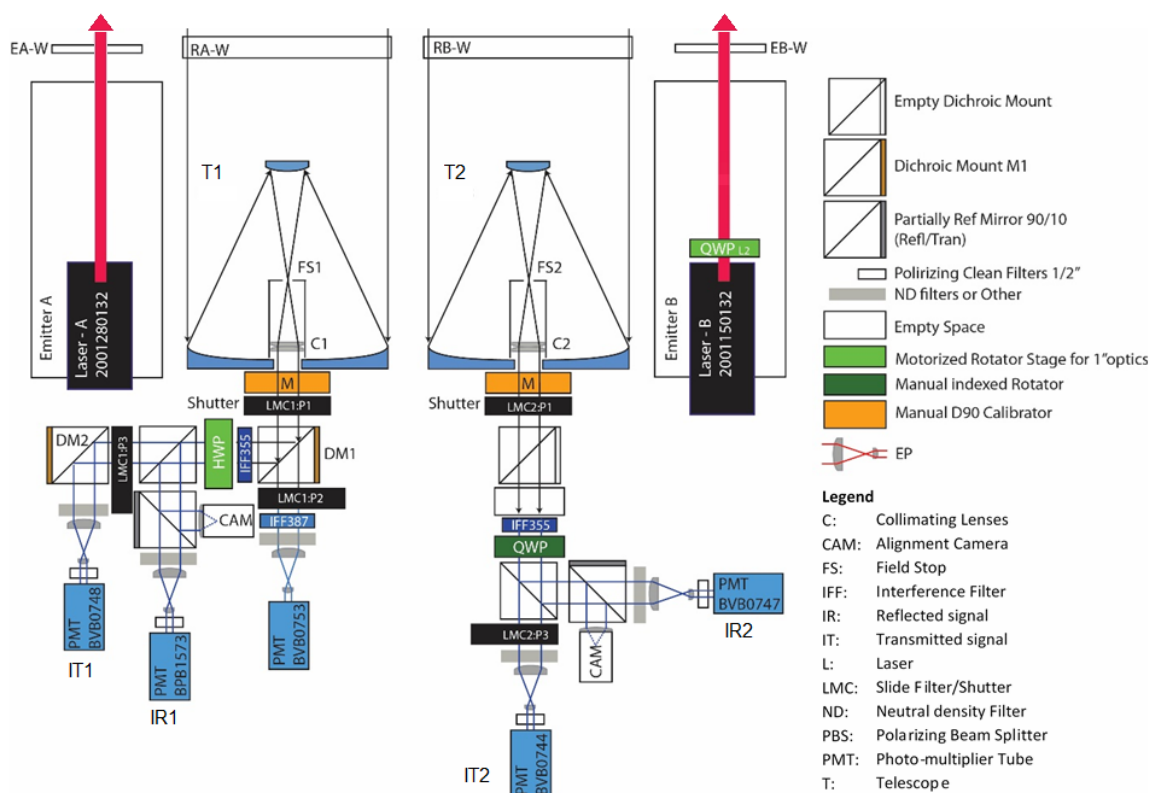


central wavelength of 386.7 nm and width of 0.9 nm, in order to isolate the inelastic vibrational Raman backscattered light from atmospheric nitrogen which is eventually collected by a PMT. An additional motorised shutter (LMC1:P2) is installed before the IFF, to protect the Raman PMT cathode from strong incident light during daytime. The reflected light goes through a 354.7 nm IFF with 0.5 nm width and a motorised rotating Half Wave Plate (HWP) before reaching the Polarising Beam Splitter cube (PBS). The PBS separates the incoming light in two orthogonal polarisation components with respect to its eigen axis. For linearly polarised emission, the PBS acts like a linear analyser and separates the parallel and cross components of the backscattered light with respect to the original laser polarisation orientation in the reflected and transmitted paths of the PBS, respectively. Due to space restrictions, a second dichroic mirror (DM2) is placed in the transmitted path of the PBS, folding the transmitted light path from the PBS towards the PMT. Finally, the beam diameter of the reflected and transmitted light is further reduced using beam reducers (eye-pieces; EPs) before being collected from the PMTs (an eye-piece is also placed before the Raman PMT). The eye-pieces are used in order to avoid distortions in the recorded signals by the inhomogeneous detection sensitivity across the active area of the PMT's cathode (Freudenthaler, 2004; Freudenthaler et al., 2018; Simeonov et al., 1999).

In WSU2, the incoming light initially passes through a 354.7 nm IFF with 0.5 nm width. Before the PBS, a QWP is placed at 45° with respect to the PBS eigen axis. The QWP along with the PBS acts as a circular analyser (Freudenthaler, 2016). For circularly polarised emission, a circular analyser separates the backscattered light to the co-polar and cross-polar components with respect to the original laser polarisation orientation in the reflected and transmitted paths of the PBS, respectively. The reflected and transmitted light from the PBS passes through the EP and then it is collected from the cathode of the PMTs.

At both WSUs, cleaning polarising filters are placed before the PMTs. These filters reduce the cross-talk effect of the PBS with a contrast ratio between the parallel and the perpendicular transmittance of 1000:1, and with this cross-talk cleaning the PBS can be considered ideal (Freudenthaler, 2016). In addition, the reflected light from the PBS goes through a partially reflecting mirror, where ~90% of the light is reflected towards a camera (CAM) for system alignment purposes, while the rest is transmitted and detected by the PMT.

The transmitted optical paths, that correspond to the cross-polar component of the collected light in both WSUs, include a detachable filter on a motorised actuator (LMC1:P3 and LMC2:P3) that is deployed during the polarisation calibration measurements. Moreover, neutral density filters can be placed in front of each PMT in order to achieve optimum signal levels.



170

**Figure 2: Schematic of the lidar head. The two lasers A and B emit linearly and circularly polarised light, respectively, whereas the two telescopes 1 and 2 along with their receiver optics (i.e., the WSU1 and WSU2) collect the elastically and inelastically backscattered light and further analyse the linear and circular polarisation of the elastically backscattered light. The analysed signals are detected by five PMTs.**

## 2.2. The alt-azimuth positioner

175

The positioner consists of two side arms and a base along with a laser on indicating beacon, as it is shown in Fig. 3. The base can rotate in azimuth and a manual break is used to keep the head fixed at the desired azimuth direction. A large worm gear reducer is used to hold the position of the head at any zenith angle. Thus, the positioner provides a manual scanning capability to the lidar, since the lidar head can be rotated to point at different zenith and azimuth angles. Due to the umbilical tubes, the positioner enables the rotation along azimuth from  $-150^{\circ}$  to  $+150^{\circ}$  and the elevation from  $-10^{\circ}$  to  $+90^{\circ}$  off-zenith.



**Figure 3: The alt-azimuth positioner with its two side arms and the base.**

### 2.3. The Electronics Enclosure

180 As shown in Fig. 4, the electronics enclosure contains a precipitation monitor, an external enclosure with DC power supplies, a dedicated lidar peripheral controller integrated with an industrial computer, two detection electronic racks (Licel GmbH), an on-line UPS, two power supplies and cooling units for the lasers, a fully programmable power distribution unit, two heat exchangers, the power cable along with the lidar's main switch, and two sockets for the umbilical tubes. The electronics enclosure is weather protected and its internal temperature is stabilized in  $30 \pm 2.5$  °C by the air to water heat exchangers.

185 The lidar peripheral controller is the unit that controls (locally or remotely) the lidar through several ethernet interfaces. In addition, the lidar peripheral controller is connected with several hardware interlocks, like the emergency button or a switch in the LH covers, for shutting down the lasers for safety reasons or in case of emergency.

Considering the two detection electronic racks, the first one contains the five Transient Recorders (TRs) along with the master trigger control unit, while the second one contains the five PMTs high voltage power suppliers. The TRs digitalize the PMT

190 signals simultaneously in analogue and photon counting mode, resulting to the acquisition of 10 signals composed by the four depolarisation plus one Raman channels in analogue and photon-counting mode. The demanding requirement on reaching the best dynamic range in the signal detection along with high temporal resolution under high repetition rates is fulfilled by means of an Analogue to Digital Converter (ADC) of 16 Bit at 40 MHz developed by Licel GmbH, (2020). The trigger control unit controls the two lasers and two receivers enabling the interleaved emission in order to avoid the interference between the pulses

195 from both lasers, and consequently the synchronization of emission and acquisition. In detail, the trigger generator firstly triggers the laser LA to start emitting outgoing light pulses and all the TRs for the acquisition of the 10 backscattered signals of both telescopes in a memory slot A of the Licel transient recorders. Then, it triggers laser LB and all the TRs for the acquisition of the rest 10 backscattered signals in a memory slot B.



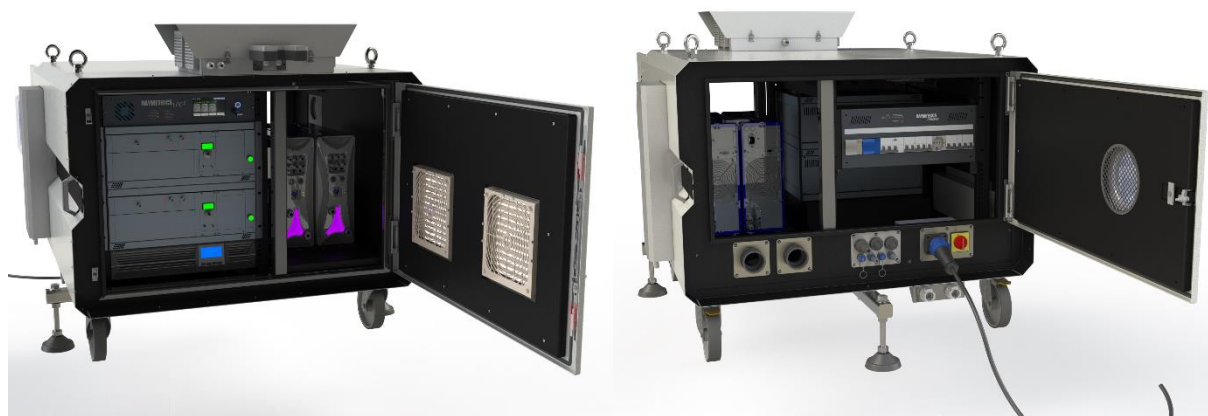


Figure 4: The front (left) and back (right) view of the electronics enclosure.

### 200 3. Polarisation calibration techniques

A relative calibration of the depolarisation channels of the eVe lidar is required (Freudenthaler, 2016; Weitkamp, 2005). An extended description on how each lidar setup is handled for calibration purposes along with techniques for aligning the polarisation plane of the emission and the optical parts with respect to the reference plane as well as for diagnosing unwanted polarising effects will be given in a follow up paper. Here, only the outcome of the applied calibration methods is provided. It has to be pointed out that for all applied methods it is assumed that the calibration measurements are performed in atmospheric layers with randomly oriented particles/molecules, because only for this case we know the theoretical distribution of the backscatter signal intensity in the two polarisation detection channels and can apply the theoretical corrections described in Freudenthaler, (2016).

The definition of the calibration methodology is facilitated with the use of the mathematical Stokes-Müller formalism for the description of the system (Chipman, 2009a). More specifically, the Stokes vectors are used to describe the polarisation state of the light (Chipman, 2009b), and the Müller matrices are used to describe how the atmosphere (van de Hulst, 1957; Mishchenko et al., 2002; Mishchenko and Hovenier, 1995) and any optical element (Lu and Chipman, 1996) can alter the polarisation state of the induced light.

As already mentioned in the previous section, the master trigger control triggers the two lasers to emit outgoing pulses interleaved and the TRs to record the received signals in a different memory slot per laser. Considering this, four emission-detection configurations are created, constituting the eVe lidar a quadruple lidar system which can also successfully calibrate itself. The four emission-detection configurations (A1, A2, B1, B2) that operate in parallel, are presented in Fig. 5.

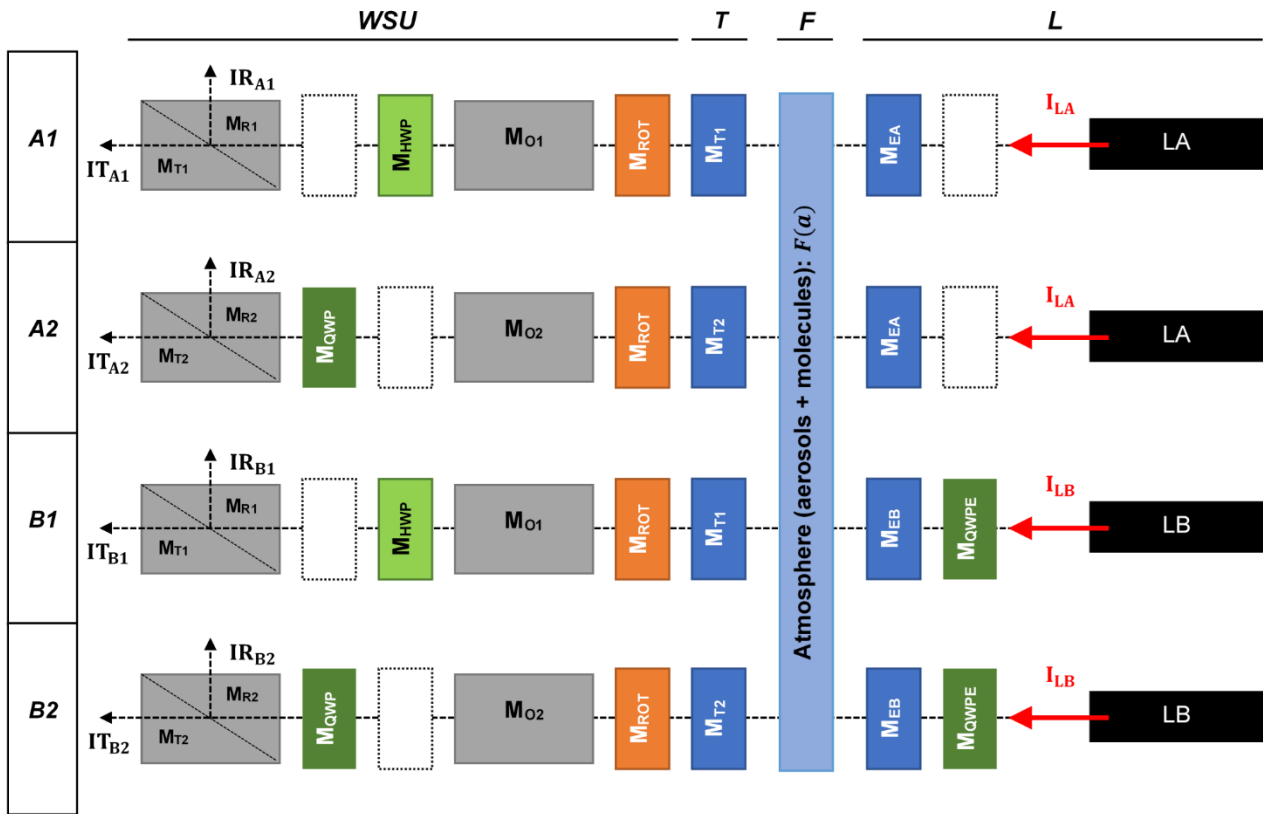


Figure 5: Sketches of the four laser-receiver configurations that are formed with the interleaved measurements of the two-laser-two-telescope setup of eVe. A1 combines the linearly polarised emission of laser LA with the linear polarisation analyser WSU1. A2 combines the linearly polarised emission of LA with the circular polarisation analyser WSU2. B1 combines the circularly polarised emission of laser LB with the linear polarisation analyser WSU1. And finally, B2 combines the circularly polarised emission of laser LB with the circular polarisation analyser WSU2. See text for further details.

220

According to Fig. 5, the emission part (L) includes the Stokes vectors of the lasers ( $I_{LA}$  and  $I_{LB}$ ), the Müller matrix of the QWP in front of LB ( $M_{QWPE}$ ), and the Müller matrices of the glass cover windows of the emitters ( $M_{EA}$  and  $M_{EB}$ ). Next in the optical path is the backscatter Müller matrix of the atmosphere ( $F(\mathbf{a})$ , where  $\mathbf{a} = F_{22}/F_{11}$  is the polarisation parameter; Chipman, 2009a; Freudenthaler, 2016). The telescope part (T) contains the combined Müller matrices of the telescope units ( $M_{T1}$  and  $M_{T2}$ ) which include the glass cover windows, the primary and secondary mirror, and the collimating lenses. The receiver part (WSU; Wavelength Separation Unit) includes the Müller matrices of the manual rotator ( $M_{ROT}$ ), the receiver optics ( $M_{O1}$  and  $M_{O2}$ ), the motorised rotating HWP ( $M_{HWP}$ ) in WSU1, the QWP ( $M_{QWP}$ ) in WSU2 that is part of the circular analyser, and the PBS including their cleaning polarisation filters for the reflected and the transmitted channels ( $M_{R1}$ ,  $M_{T1}$  and  $M_{R2}$ ,  $M_{T2}$ ). After the PBS, the corresponding Stokes vectors of the light in the reflected and transmitted path of the PBS are given ( $IR_{ij}$  and  $IT_{ij}$ , respectively, where  $i = A, B$  and  $j = 1, 2$ ) considering the four lidar combinations.

230



The laser emission at 355 nm is highly polarised with a degree of linear polarisation (DOLP) of 0.997 and 0.998 for LA and LB, respectively, which has been measured in the laboratory. The emission optics have been tested and they do not introduce any significant polarising effects, thus their matrices ( $M_{EA}$  and  $M_{EB}$ ) are presented by the identity matrix (Chipman, 2009a). The same applies also for the matrices of the telescope optics ( $M_{T1}$  and  $M_{T2}$ ). Regarding the receiver optics, the only part that could introduce diattenuation or retardance is the dichroic beam splitter in WSU1 ( $M_{O1}$ ). According to Freudenthaler, (2016), it can be modelled as a non-rotated retarding diattenuator and because of the manufacturing accuracy it is not rotated. The cleaned PBS and all waveplates are considered ideal and their expressions for a given rotation angle can be also found in Freudenthaler, (2016). On the other hand, the receiver optics in WSU2 ( $M_{O2}$ ) mainly includes the interference filter and the collimating lenses (C2), both of which are not expected to change the state of polarisation. In addition, the PBS incidence plane of the respective WSU is selected as the polarisation reference plane and all rotational optical parts (QWPE, HWP, QWP) are accurately aligned by means of motorised rotation mounts with respect to this plane. The motorised rotation mounts have a minimum incremental motion of  $0.001^\circ$  and a bi-directional repeatability of  $0.003^\circ$ .

The alignment of the polarisation plane of the emitters with the reference plane is also necessary, at least for the linearly polarised emission with respect to the linear analyser in WSU1, since the circularly polarised emission and the circular analyser in WSU2 are independent of rotation. For that reason, the manual rotator in the WSU1 can be used to align the emitter A with the WSU1 according to Freudenthaler, (2016) section 11.

The configurations A1 and B2 are used to obtain the volume linear and volume circular depolarisation ratios, respectively, as well as the backscatter and extinction coefficients from the two polarised emissions, while the other two configurations, A2 and B1, are used for calibration purposes and also to diagnose unwanted polarising effects in the system.

### 3.1. Calibration factor in WSU1

When normal measurements are performed with configuration A1, the parallel and cross polarised components are detected in the reflected and transmitted optical paths of the linear analyser, respectively, aiming to reduce the cross-talk errors even more (Freudenthaler et al., 2009). The calibrated signal ratio of the reflected and transmitted channels, which is defined in Freudenthaler, (2016), Eq. (60) can be written as:

$$\delta_{A1}^* = \frac{1}{\eta_1} \cdot \frac{I_{R,A1}}{I_{T,A1}} = \frac{1+D_{O1}}{1-D_{O1}} \cdot \frac{1}{\delta_{lin}^v} \quad (1)$$

where  $\eta_1$  is the calibration factor that corresponds to the relative amplification of the reflected ( $I_{R,A1}$ ) and the transmitted ( $I_{T,A1}$ ) channels,  $D_{O1}$  is the diattenuation parameter of the receiver optics (Freudenthaler, 2016; supplement section S.4), and  $\delta_{lin}^v$  is the volume linear depolarisation ratio of the atmosphere. Once the calibration factor and the diattenuation parameter of the receiver optics are determined, the volume linear depolarisation ratio can be retrieved.

The calibration factor ( $\eta_{1,HWP}$ ) is determined with configuration A1 by means of the  $\Delta 90$ -calibration method using the HWP in front of the PBS (Freudenthaler, 2016; section 7.1). It does not include the polarisation effects of optical parts before the



HWP. That's why the correction for the diattenuation in Eq. (1) is necessary. The calibration measurements are performed by  
 265 rotating the HWP at  $\pm 22.5^\circ$  with respect to its zero position, which corresponds to the rotation of the linear polarisation  
 orientation of the incident light by  $\pm 45^\circ$  with respect to the PBS incidence plane. The calibration factor ( $\eta_1$ ) that is calculated  
 from the geometrical mean of the two gain ratios ( $\eta_{A1}^*(\pm 45^\circ)$ ) of the calibration signals ( $\Delta 90$ -calibration), is independent of a  
 rotational offset of the HWP:

$$\eta_{1\_HWP} = \sqrt{\eta_{A1}^*(+45^\circ) \cdot \eta_{A1}^*(-45^\circ)} = \sqrt{\frac{I_{R,A1}(+45^\circ)}{I_{T,A1}(+45^\circ)} \cdot \frac{I_{R,A1}(-45^\circ)}{I_{T,A1}(-45^\circ)}} \quad (2)$$

The diattenuation effect of the receiver optics ( $D_{O1}$ ) can be determined by performing an additional  $\Delta 90$ -calibration using the  
 270 manual rotator of the WSU1 before the receiver optics at  $\pm 45^\circ$  (Belegante et al., 2018; Freudenthaler, 2016), which yields the  
 calibration factor  $\eta_{1\_manual}$ . From the ratio of the two calibration factors, we can retrieve the diattenuation parameter of the  
 receiver optics ( $D_{O1}$ ) using Eq. (3) (Belegante et al., 2018; Freudenthaler, 2016):

$$\frac{\eta_{1\_manual}}{\eta_{1\_HWP}} = \frac{1+D_{O1}}{1-D_{O1}} \quad (3)$$

With this technique  $D_{O1}$  was found to be  $0.000 \pm 0.011$ .

Upon the determination of  $D_{O1}$ , the calibration factor can be also calculated using the configuration B1 by performing directly  
 275 normal measurements, i.e., without any rotation of the calibrators. It has to be pointed out that this calibration procedure can  
 be applied only in case the receiver optics does not produce retardation effects, which has to be verified first. The gain ratio  
 ( $\eta_{B1}^*$ ) of the measured reflected and transmitted signals from B1 ( $I_{R,B1}$  and  $I_{T,B1}$ ) is identical to  $\eta_{A1}$ .

### 3.2. Calibration factor in WSU2

When normal measurements are performed with configuration B2, the co- and cross-polar components of the backscattered  
 280 signal are detected in the reflected and transmitted optical paths of the circular analyser, respectively, like in configuration A1  
 above. The calibrated signal ratio of the reflected and transmitted channels can be written as:

$$\delta_{B2}^* = \frac{1}{\eta_2} \cdot \frac{I_{R,B2}}{I_{T,B2}} = \frac{1}{\delta_{cir}^v} \quad (4)$$

where  $\eta_2$  is the relative calibration factor between the reflected ( $I_{R,B2}$ ) and transmitted ( $I_{T,B2}$ ) channels and  $\delta_{cir}^v$  is the volume  
 circular depolarisation ratio. Once the calibration factor is determined, the volume circular depolarisation ratio can be directly  
 calculated.

285 Here, the calibration factor can be easily determined with any combination of linear and unpolarised light, since the linearly  
 polarised light, regardless of its rotational angle, is split in half by the circular analyser in WSU2 and there are no additional  
 polarising elements in the optical path before the circular analyser. Thus, the configuration A2 can be used directly, without  
 any adjustment, for the determination of the calibration factor  $\eta_2$ . The gain ratio ( $\eta_{A2}^*$ ) of the measured signals is equal to the  
 calibration factor ( $\eta_2$ ) in Eq. (5).

$$\eta_{A2}^* = \frac{I_{R,A2}}{I_{T,A2}} = \eta_2 \quad (5)$$



290 Configuration B2 can be used in the same way for the determination of the calibration factor  $\eta_2$ , by adjusting the motorised QWPE so that it is at  $0^\circ$  with respect to the original linear polarisation of laser LB, resulting in the emission of linearly polarised light from emitter B. The B2 configuration is preferred against the A2 configuration, because the alignment of the dual-laser/dual-telescope system is optimum for the A1 and B2 configurations. Equation (5) is also valid for the measured signals from the adjusted B2 configuration.

## 295 **4. Signal processing software and retrieved products**

A processing software has been developed for the analysis of the recorded signals and the corresponding retrieval of the optical products. The required inputs are raw lidar signals and ancillary information regarding the lidar configuration (location's coordinates, measurement zenith and azimuth angles) and the atmospheric conditions (temperature, pressure, and humidity) under which the measurements were performed. The retrieved aerosol optical products are the particle backscatter coefficient, the particle extinction coefficient, the volume and particle linear depolarisation ratios as well as the volume and particle circular depolarisation ratios at 355 nm. The software is divided in two modules, the pre-processing chain and the aerosol optical product processing chain. In addition, the software is capable of analysing signals from the dark measurements (Freudenthaler et al., 2018) and during quality assurance and quality control tests proposed by EARLINET, such as the telecover test, the Rayleigh-fit test, and the polarisation calibration (Freudenthaler et al., 2018).

### 305 **4.1. Pre-processing chain**

The pre-processing chain handles the raw signals that will be used for the retrieval of the aerosol optical products. Since the raw lidar signals are recorded in both photon-counting and analogue modes, the following corrections are applied. First of all, the photon-counting signals are corrected for the dead-time introduced by the PMT and the photon counter electronics (Donovan et al., 1993; Evans, 1955). Then, in order to increase the signal-to-noise ratio (SNR), the signals are averaged in time, using a time window which is also representative of the corresponding atmospheric conditions. After time averaging, the atmospheric background that correspond to an offset value, is subtracted from the signals. The background signal introduced by the electronics in analogue detections is subtracted from the corresponding analogue signals as well. The pre-trigger region is preferred for the calculation of the background offset value in order to avoid the small but not negligible contribution of the atmospheric backscatter at the far end of the signal. The pre-trigger region is then corrected for the signals, considering also any trigger delay between the outgoing laser pulse and the time that the TRs actually start recording the backscattered signals, which can be determined according to the trigger delay test in (Freudenthaler et al., 2018). To further increase the SNR, the signals are vertically smoothed by means of a polynomial fit with the capabilities of defining the polynomial order, as well as the length of the smoothing window which can be fixed (see D'Amico et al., 2016) or variable (see Ansmann et al., 1992; Wandinger and Ansmann, 2002).



320 After the vertical smoothing, the analogue and photon-counting signals per channel are “glued” in order to produce a combined  
signal with increased dynamic range compared to the individual ones. Eventually the signals are corrected for the range  
dependence of the recorded signal profile (Weitkamp, 2005). In addition, the algorithm is capable of applying a correction in  
the signals for incomplete overlap. The overlap profile can be obtained following the methodology proposed by Wandinger  
and Ansmann, (2002). In the case of eVe lidar which has scanning capabilities a sensitivity study must be performed on the  
325 overlap function in order to investigate whether the overlap profile is stable over time and over multiple measurement angles.  
This sensitivity study has not been conducted yet, thus the processed signals are not overlap corrected.

For each WSU, the pre-processed corrected signals from the co-polar and cross-polar components are combined to construct  
a new signal, defined as the calibrated sum of the respective polarised components according to Freudenthaler, (2016), Eq.  
(65). The calibrated sum signal is proportional to the total signal that would have been recorded if the beam had not been split  
330 with the PBS.

In analogue signals, the electronic noise can produce range dependent artifacts that cannot be removed through the background  
subtraction from the signal (Freudenthaler et al., 2018). The processed analogue signals can be corrected from these range  
dependent artifacts using the signals acquired from a dark measurement, which is performed with fully covered telescopes  
before each normal measurement. The same processing procedure is applied in the dark measurement signals and then they  
335 are subtracted from the normal measurement signals.

## 4.2. Optical products processing chain

In the aerosol optical product processing chain, the desired optical products are retrieved using the pre-processed lidar signals.  
Before the products retrieval, the molecular profiles of the backscatter and extinction coefficients are calculated using the  
temperature and pressure profiles and appropriate conversion factors (Freudenthaler et al., 2018). The temperature and pressure  
340 profiles that are acquired from the nearest launched radiosonde or from a numerical weather prediction model (NWP); if none  
is available, a standard atmospheric model (e.g., the U.S. Standard Atmosphere) is used instead, adapted to the surface  
temperature, pressure, and humidity values at the measurement site. Finally, the measured signal profiles ( $I(z)$ ) along with the  
theoretical molecular profiles ( $N(z)$ ,  $\alpha^m(z)$ ) are used for the retrieval of the following optical properties.

### 4.2.1. Particle extinction coefficient

345 The particle extinction coefficient ( $\alpha^p$ ) profile is retrieved according to the Raman inversion method using the inelastic  
backscattered signal (Ansmann et al., 1992):

$$\alpha^p(z, \lambda_0) = \frac{\frac{d}{dz} \left[ \ln \frac{N(z, \lambda_{RA})}{I(z, \lambda_{RA})} - \alpha^m(z, \lambda_{RA}) - \alpha^m(z, \lambda_0) \right]}{1 + \left( \frac{\lambda_0}{\lambda_{RA}} \right)^k} \quad (6)$$

where  $z$  is the range (i.e. distance from lidar),  $I(z, \lambda_{RA})$  is the inelastic signal,  $N(z, \lambda_{RA})$  is the nitrogen molecule number  
density,  $\alpha^m(z, \lambda_0)$  is the molecular extinction coefficient for the laser wavelength  $\lambda_0$ ,  $\alpha^m(z, \lambda_{RA})$  is the molecular extinction



coefficient for the Raman wavelength  $\lambda_{RA}$ , and  $k$  is the Ångstrom exponent which is assumed to be known and constant  
 350 (ideally the value is taken from nearby AERONET measurements). According to Ansmann et al., (1992), a deviation of the  
 Ångstrom exponent from its true value in the order of 1 can cause a relative error of less than 4 % in the retrieval. The particle  
 extinction coefficient is a night-time only product as skylight hinders the detection of the weak Raman signal. The Raman  
 channel can record Raman backscattered signals from both lasers, thus the extinction coefficient of both linearly and circularly  
 polarised emitted light can be calculated independently.

#### 355 4.2.2. Particle backscatter coefficient

The Raman inversion method (Ansmann et al., 1992) can be also used for nighttime measurements to retrieve the particle  
 backscatter coefficient ( $\beta^p$ ) profile using both the elastic and inelastic backscatter signals,  $I(z, \lambda_0)$  and  $I(z, \lambda_{RA})$ , respectively.

$$\beta^p(z, \lambda_0) = -\beta^m(z, \lambda_0) + [\beta^p(z_0, \lambda_0) + \beta^m(z_0, \lambda_0)] \cdot \frac{I(z, \lambda_0) I(z_0, \lambda_{RA}) N(z, \lambda_{RA})}{I(z_0, \lambda_0) I(z, \lambda_{RA}) N(z_0, \lambda_{RA})} \cdot \frac{\exp[-\int_{z_0}^z [\alpha^p(z', \lambda_{RA}) + \alpha^m(z', \lambda_{RA})] dz']}{\exp[-\int_{z_0}^z [\alpha^p(z', \lambda_0) + \alpha^m(z', \lambda_0)] dz']}$$
(7)

where  $\beta^m(z, \lambda_0)$  is the molecular backscatter coefficient profile at any range  $z$  and  $\beta^m(z_0, \lambda_0)$  is the value of the molecular  
 backscatter coefficient at the reference range  $z_0$ . The reference range corresponds to a molecular region and it is selected  
 360 manually by visually inspecting the Rayleigh fit (Freudenthaler et al., 2018) between the pre-processed signals and the  
 attenuated molecular backscatter coefficient.

In absence of inelastic backscatter signals, as for example for daytime conditions, the particle backscatter coefficient is obtained  
 with the Klett-Fernald-Sassano (hereafter Klett) inversion method (Fernald, 1984; Klett, 1981; Sasano and Nakane, 1984)  
 using only the elastic backscatter signals. The inversion assumes a height constant particle lidar ratio  $L^p$ , and a priori  
 365 knowledge of the backscatter coefficient  $\beta(z_0, \lambda)$  at the reference range  $z_0$ . Under these assumptions, the lidar equation for  
 elastic backscatter signals can be solved by means of boundary conditions if handled like a differential Bernoulli equation. The  
 solution of the total backscattering coefficient at a wavelength  $\lambda$  can be written as:

$$\beta^p(z) = -\beta^m(z) + \frac{I(z) \cdot \exp[-2 \cdot (L^p - L^m) \cdot \int_{z_0}^z \beta^m(z') dz']}{\frac{I(z_0)}{\beta^m(z_0) + \beta^p(z_0)} - 2 \cdot L^p \cdot \int_{z_0}^z I(z') \cdot \exp[-2 \cdot (L^p - L^m) \cdot \int_{z_0}^{z'} \beta^m(z'') dz''] dz'}$$
(8)

where  $L^m$  is the molecular lidar ratio.

#### 4.2.3. Volume depolarisation ratios

370 According to Freudenthaler, (2016) the calibrated signal ratio between the reflected and transmitted channels of an analyser  
 (linear or circular) can be expressed as a function of the height dependent atmospheric polarisation parameter  $a$  and the  
 constant system parameters  $G_S$  and  $H_S$  ( $S = R, T$ ):

$$\delta^* = \frac{1}{\eta} \cdot \frac{I_R}{I_T} = \frac{G_R + aH_R}{G_T + aH_T}$$
(9)



375 The  $G_S$  and  $H_S$  parameters are used to describe the polarisation cross-talk effects in the system that depend on the state of the laser polarisation, on the diattenuation and/or retardation of the optical elements in both the emission and receiver units, as well as their relative rotation with respect to the reference plane. As a result, the  $G_S$  and  $H_S$  parameters differ for each one of the four configurations of eVe.

The polarisation parameter  $a$  can be retrieved from Eq. (9):

$$a = \frac{\delta^* G_T - G_R}{H_R - \delta^* H_T} \quad (10)$$

The volume linear depolarisation ratio is retrieved through Eq. (A12) using the calibrated signal ratio of the A1 configuration ( $\delta_{A1}^*$ ) from Eq. (1) and the polarisation parameter  $a$  from Eq. (10):

$$\delta_{lin}^v = \frac{1-a}{1+a} = \frac{\delta_{A1}^* (G_{T,A1} + H_{T,A1}) - (G_{R,A1} + H_{R,A1})}{(G_{R,A1} - H_{R,A1}) - \delta_{A1}^* (G_{T,A1} - H_{T,A1})} \quad (11)$$

380 The volume circular depolarisation ratio is retrieved through Eq. (A13) using the calibrated signal ratio of the B2 configuration ( $\delta_{B2}^*$ ) from Eq. (4) and the polarisation parameter  $a$  from Eq. (10):

$$\delta_{cir}^v = \frac{1-a}{a} = \frac{\delta_{B2}^* (G_{T,B2} + H_{T,B2}) - (G_{R,B2} + H_{R,B2})}{G_{R,B2} - \delta_{B2}^* G_{T,B2}} \quad (12)$$

#### 4.2.4. Particle depolarisation ratios

According to Beyerle, (1994), the particle linear depolarisation ratio profile can be calculated from the following equation where  $j = lin, cir$

$$\delta_j^p = \frac{(1 + \delta_j^m) \delta_j^v \mathcal{R} - (1 + \delta_j^v) \delta_j^m}{(1 + \delta_j^m) \mathcal{R} - (1 + \delta_j^v)} \quad (13)$$

385 and using the profiles of the volume linear depolarisation ratio ( $\delta_{lin}^v$ ) and the total backscatter to molecular backscatter ratio ( $\mathcal{R}$ ), and the molecular linear depolarisation ratio value ( $\delta_{lin}^m$ ). Equation (13) can be also used for the calculation of the particle circular depolarisation ratio profile by using the volume and molecular circular depolarisation ratios instead ( $\delta_{cir}^v$  and  $\delta_{cir}^m$ ) and assuming a circular polarisation in the methodology of Beyerle, (1994).

#### 4.3. Statistical uncertainty estimation

390 The estimation of statistical uncertainty of each retrieved optical product from the software is based on the Monte Carlo simulations (Robert and Casella, 2010). The Monte Carlo method consists of repeated retrievals, each time varying the input data (lidar signals) randomly within their stated limits of precision. If a realistic error can be simulated for the input data, then, the final optical product error distribution and standard error can be estimated. A benefit of this technique is that no assumptions are required during error propagation (e.g., assuming uncorrelated errors). A more detailed description on the application of the Monte Carlo method in the calculation of the statistical uncertainty in the retrieved products is given in D'Amico et al., (2016) and Mattis et al., (2016).





#### 4.4. Algorithm intercomparison

The algorithms for the processing of the lidar data have been tested using the synthetic lidar dataset which has been created for the algorithm inter-comparison exercise performed in the framework of EARLINET (Böckmann et al., 2004; Pappalardo et al., 2004). In brief, the dataset contains a 30 min time series of synthetic raw lidar signals simulated assuming realistic experimental and atmospheric conditions. Both elastic (at 355 nm) and N<sub>2</sub> Raman (at 387 nm) raw lidar signals are taken into account to reproduce as much as possible a real measurement sample of a typical advanced multi-wavelength Raman lidar with an incomplete overlap between the laser and the receiver field of view below 300 m. The synthetic signals were processed with the developed software for eVe products (eVe software) and are shown in Fig. 6, where a vertical smoothing with a first order polynomial fit and a smoothing window of 100 m was applied. In addition, the signals were not corrected for the incomplete overlap and the reference height of molecular region was selected at 6.5 km altitude within a 0.5 km window.

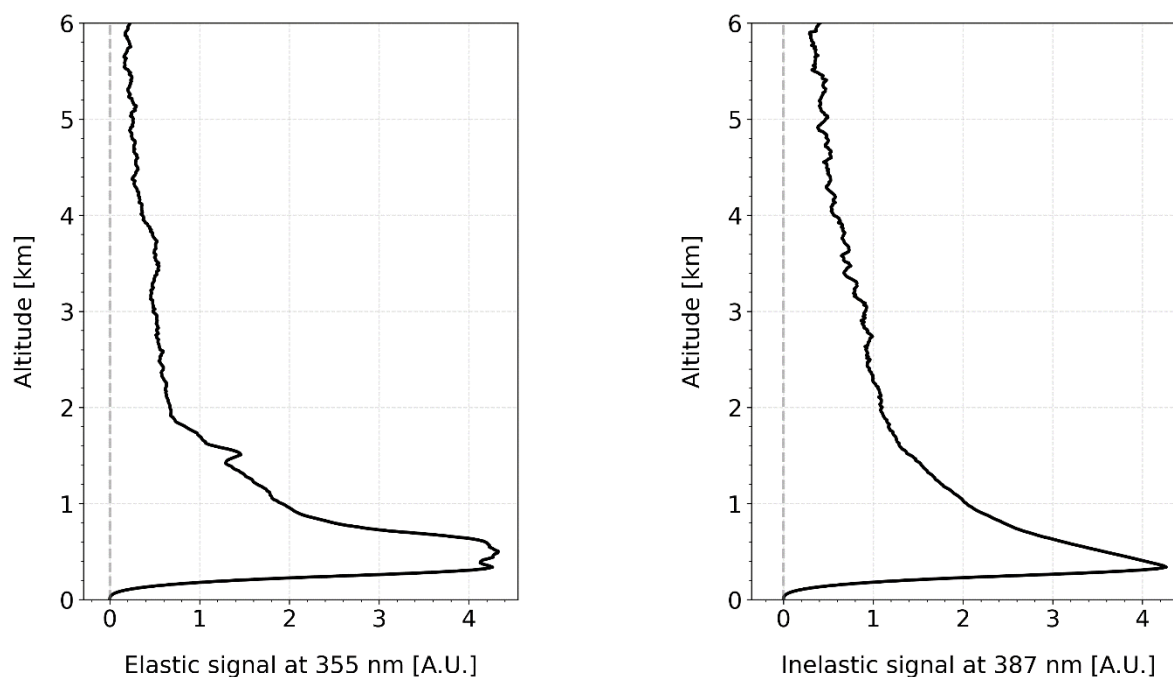
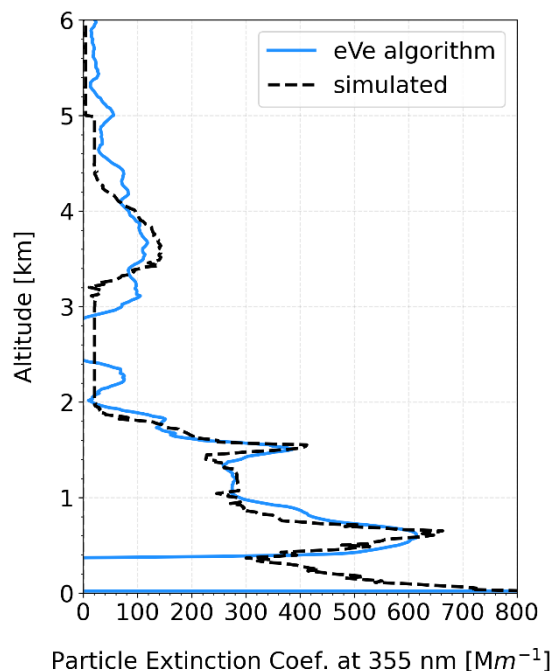


**Figure 6:** The synthetic elastic and inelastic signal profiles at 355 nm and 387 nm, respectively, that were used as an input in the eVe software. The signals are range-corrected and vertically smoothed with a first order polynomial fit and a smoothing window of 100 m.

The particle backscatter and extinction coefficients at 355 nm were retrieved in order to be compared with the simulated ones. The backscatter coefficient was retrieved using both the Raman and the Klett inversion methods, where for the latter, a height-constant aerosol lidar ratio of 60 sr, which is known a priori from the simulation, was used. The following figures 7 and 8 show the intercomparison between the simulated and the retrieved coefficients. For the statistical analysis of the intercomparison, the bias was calculated as the absolute difference between the simulated and the retrieved profile has been calculated using the simulated profile as reference. The mean bias and the respective standard error were calculated inside



three selected altitude regions from Pappalardo et al., (2004) and are provided in Table 1 for the particle extinction coefficient and in Table 2 for the particle backscatter coefficient. The first region extends from 0.35 to 2 km representing typical aerosol load inside the planetary boundary layer, the second region that is aerosol free extends from 2 to 3 km, and the third region extends from 3 to 4.4 km where an elevated aerosol layer is present.



420 **Figure 7: Comparison of the extinction coefficient profile at 355 nm retrieved by means of the eVe software (solid; blue) and the simulated profile (dashed; black).**

In Fig. 7, below 0.35 km the retrieved profile is affected by the incomplete overlap that is present in the processed synthetic signals and the retrieval inside this range region will be not taken into consideration for the intercomparison. Overall, the retrieved extinction coefficient profile shows a good agreement with the simulated profile. In the first height range (0.35 – 2 km) the mean bias between the retrieved and the simulated extinction profile is 13.84  $Mm^{-1}$  falling within the 23  $Mm^{-1}$  that was found for the majority of the stations in Pappalardo et al., (2004). In the elevated aerosol layer (3 – 4.4 km) the mean bias is 11.05  $Mm^{-1}$  and agrees well with the bias of 13  $Mm^{-1}$  that was found in the majority of the stations in Pappalardo et al., (2004). In the aerosol free height range (2 – 3 km) the mean bias is -8.83  $Mm^{-1}$  denoting a trend of underestimation with respect to the majority of the stations in Pappalardo et al., (2004) where the bias is below 17  $Mm^{-1}$  and 45 % of the stations have underestimation trends.

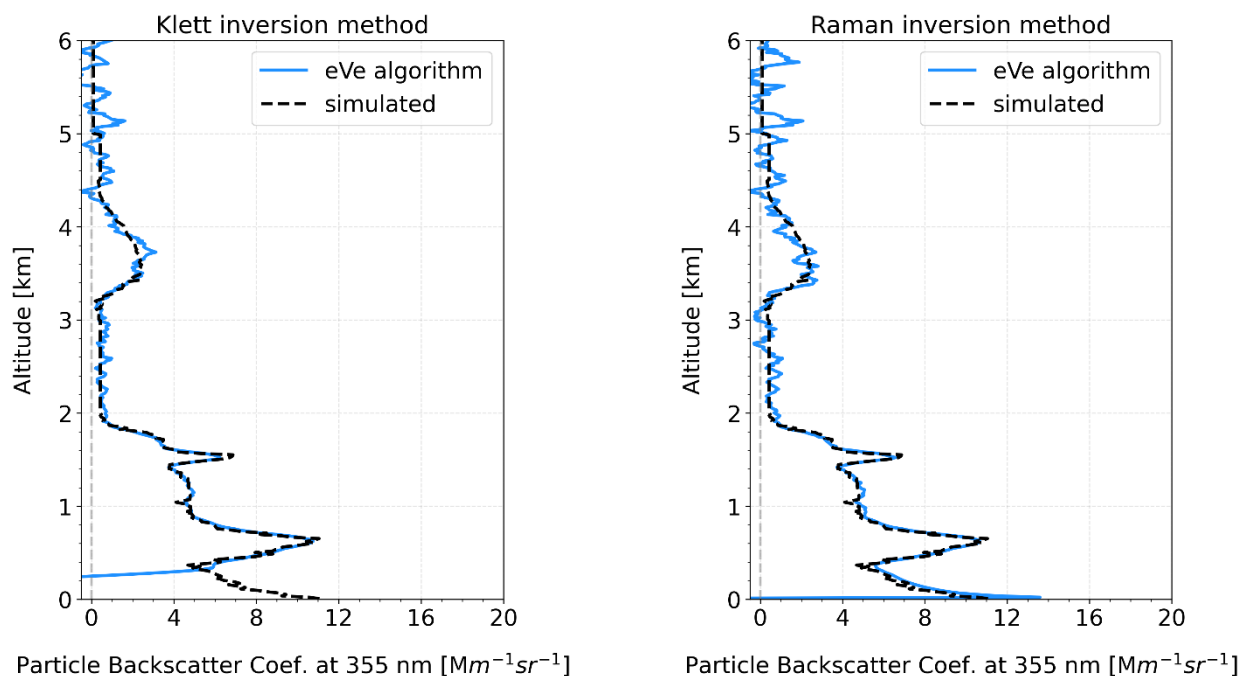
**Table 1: Mean bias and standard error of the particle extinction coefficient for three altitude ranges**

Altitude range (km)	Mean bias ( $Mm^{-1}$ )	Standard error	Mean simulated value ( $Mm^{-1}$ )
0.35 – 2	13.84	84.37	300.31



2 – 3	-8.83	42.38	20.71
3 – 4.4	11.05	37.42	81.11

In the height range from 2 to 3 km, the retrieval is noisier leading to an inaccurate representation of the molecular region. The combination of the weak and noisy Raman signal along with the low extinction values due to molecular region can cause distortions in the differentiation in Eq. (6); the distortions can be further enhanced or removed depending of the selected derivative window for the differentiation. The artificial noise that was inserted in the synthetic signals (Fig. 6) was customized to simulate the higher levels of noise from older lidar signal recorders compared to the ones deployed on EVE. Hence, in such altitudes ranges, the lidar signals from eVe have a better SNR compared to the synthetic signals, resulting to a less noisy as well as more reliable retrieval of the extinction coefficient profile.



440 **Figure 8: Comparison of the backscatter coefficient profile at 355 nm retrieved from the eVe software (solid; blue) and the simulated profile (dashed; black). The backscatter profile was retrieved using the Klett (left) and the Raman (right) inversion method.**

The backscatter coefficient profiles retrieved from both inversion methods compared to the simulated one, show a rather good agreement, consistent with the most EARLINET algorithms in all altitude ranges as shown in Fig. 8. In the first height range (0.35 – 2 km) in Table 2 the mean bias for the Klett solution is  $0.069 \text{ Mm}^{-1}\text{sr}^{-1}$  and for the Raman solution is  $0.11 \text{ Mm}^{-1}\text{sr}^{-1}$  when the bias for most of the stations in Pappalardo et al., (2004) is below  $-0.54 \text{ Mm}^{-1}\text{sr}^{-1}$ . In the elevated aerosol layer (3 – 4.4 km) the retrieved profile seems to be underestimated with respect to the simulated profile with the mean bias for the Klett and Raman solutions to be  $-0.03$  and  $-0.16 \text{ Mm}^{-1}\text{sr}^{-1}$ , respectively, falling well within the mean bias of  $-0.40 \text{ Mm}^{-1}\text{sr}^{-1}$  that is found in most of the rest intercomparison stations. Last but not least, in the aerosol free region (2 – 3 km) the mean bias for



the Klett and Raman solutions is  $0.13$  and  $0.06 \text{ Mm}^{-1}\text{sr}^{-1}$ , respectively, while the for the majority of the intercomparison stations  
 450 the mean bias is below  $-0.30 \text{ Mm}^{-1}\text{sr}^{-1}$ .

Below the  $0.3 \text{ km}$  where the full overlap height is defined, the underestimation of the Klett solution with respect to the Raman  
 solution is highlighted, since with Raman method a backscatter coefficient profile can be obtained without the dependence of  
 the overlap function as it is cancelled out in the ratio of the lidar signals in Eq. (7).

455 **Table 2: Mean bias and standard error of the particle backscatter coefficient retrieved with the Klett and the Raman inversion  
 methods for three altitude ranges**

Altitude range (km)	Mean bias ( $\text{Mm}^{-1}\text{sr}^{-1}$ )		Standard error		Mean simulated value ( $\text{Mm}^{-1}\text{sr}^{-1}$ )
	Klett	Raman	Klett	Raman	
0.35 – 2	0.069	0.11	0.34	0.33	5.06
2 – 3	0.13	0.06	0.16	0.29	0.43
3 – 4.4	-0.03	-0.16	0.32	0.41	1.35

Overall, the profile from the Klett solution shows better agreement with the simulated one, compared to the noisier profile  
 obtained from the Raman solution. In principle, the Raman solution is expected to be noisier, since the elastic and inelastic  
 460 signals that are used, insert two different uncertainties in the retrieval, while only the elastic signal is used for the Klett solution.  
 On the other hand, the Klett solution strongly depends on the user defined value of lidar ratio. For the intercomparison, the  
 lidar ratio value which was used in the algorithm, was provided with the simulation signals, resulting in an optimum retrieval  
 of the backscatter coefficient profile. Thus, if an inaccurate lidar ratio was used instead, the retrieved profile would deviate  
 more from the simulated one.

465 **5. eVe first measurements**

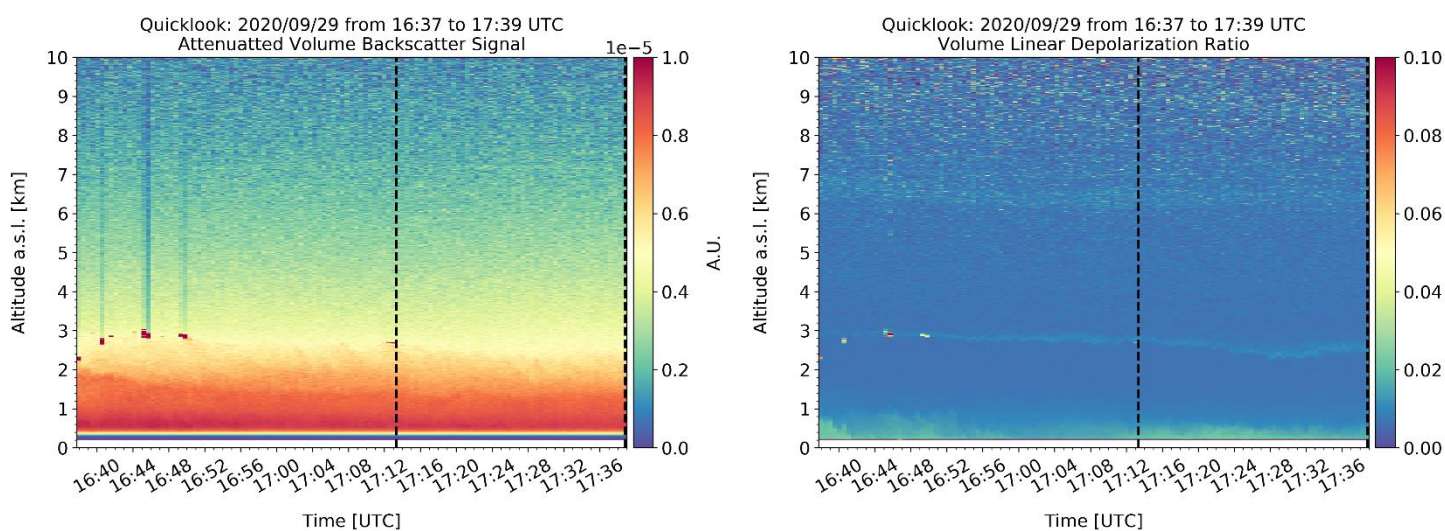
Two selected measurement cases are presented from the first conducted measurements of eVe lidar. The system was located  
 in Athens, Greece ( $38.06^\circ \text{ N}$ ,  $23.75^\circ \text{ E}$ ) at an elevation of  $194 \text{ m}$  above sea level. For each case, a vertical smoothing with a  
 first order polynomial fit and a smoothing window of  $100 \text{ m}$  was applied in the measured signals and they were not corrected  
 for the incomplete overlap. The retrieved optical products are the particle backscatter coefficient, the particle extinction  
 470 coefficient, the volume and particle linear depolarisation ratios (VLDR and PLDR), as well as the volume and particle circular  
 depolarisation ratios (VCDR and PCDR). The retrieved VLDR and PLDR were used in order to reproduce the VCDR and  
 PCDR, respectively, using the theoretical relationship between them ( $\delta_{cir} = 2\delta_{lin}/(1 - \delta_{lin})$ ; Mishchenko and Hovenier,  
 1995; Roy and Roy, 2008). The comparison of the retrieved VCDR and PCDR with the converted ones (i.e., the VLDR-to-  
 VCDR and the PLDR-to-PCDR) can indicate particle orientation and/or multiple scattering if they do not agree (see Appendix  
 475 A). In the Appendix A we examined whether the theoretical relationship between the linear and the circular depolarisation



ratios can be used with the backscatter coefficient retrieved from ground-based polarisation lidar systems to retrieve a product that is comparable with the Aeolus backscatter coefficient for the validation of the Aeolus L2A products. Hence, the ‘Aeolus like’ backscatter coefficient was calculated, using the retrieved particle backscatter coefficient from the circularly polarised emission and the eq. (A15) from Appendix. In this study, the ‘Aeolus like’ backscatter coefficient corresponds to the particle  
480 backscatter coefficient that Aeolus would measure from ground, if Aeolus and eVe were pointing at the same atmospheric volume.

### 5.1. Case study of 29 September 2020

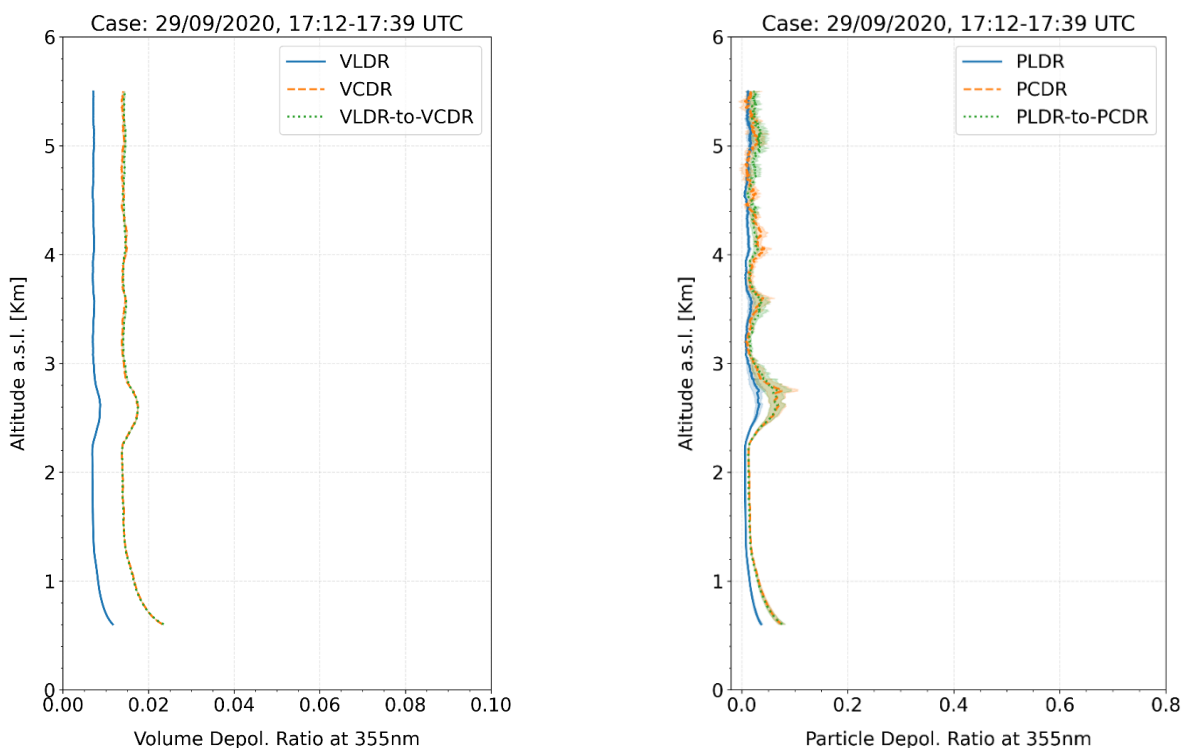
Figure 9 gives an overview of the performed measurements on 29 September 2020, from 16:37 to 17:39 UTC. Traces of low clouds are present at approximately 3 km, between 16:37 and 16:48 UTC, and around 17:10 UTC at both attenuated volume  
485 backscatter signal and VLDR profiles. In addition, a very thin depolarising layer can be observed in the scene, through the VLDR profile, initially located at 3km and then, as the time passes, at approximately 2.6 km. Elevated layers with depolarising particles are present in the scene, at approximately 6.5 and 9 km. Moreover, depolarising particles are also detected inside the PBL (below 1 km) but they are not form a persistent layer, due to the strong winds that blew that day. These particles originated from a local dust emission from industrial activities near the location where the lidar was placed.  
490 The timeframe from 17:12 to 17:39 UTC, enclosed by the black dashed lines in Fig. 9, was selected for the retrieval of the aerosol optical products. Inside this timeframe, both attenuated volume backscatter signal and VLDR profiles denote a rather clear atmospheric scene up to 10 km, expect of the minor depolarising layer which is detectable at approximately 2.6 km.



495 **Figure 9: Height versus time plots of the attenuated volume backscatter signal from linear emission and the volume linear depolarisation ratio at 355 nm over Athens, measured by eVe lidar on 29 September 2020 from 16:37 to 17:39 UTC. The raw temporal and vertical resolution are 30 s and 3.75 m, respectively, with vertical pointing of the system. The attenuated volume backscatter signal was calibrated using a calibration factor averaged inside the selected timeframe and calculated at 3.8 km with a 0.3 km window. The two back dashed lines enclose the selected timeframe for the optical products retrieval.**



Figures 10 and 11 show the optical products retrieved from the signals averaged over the selected timeframe. The suspended particles in the atmosphere are slightly depolarising, according to the VLDR profile in Fig. 10 (left), since no values larger than the  $0.011 \pm 0.000$  and  $0.008 \pm 0.000$  are observed below 1.2 km and at approximately 2.6 km, respectively. Figure 10 shows the VCDR profile as well as the converted volume circular depolarisation ratio profile (VLDR-to-VCDR), where both the VCDR and VLDR-to-VCDR values are up to  $0.022 \pm 0.000$  below 1.2 km and up to  $0.017 \pm 0.000$  at approximately 2.6 km. It is obvious that the VLDR-to-VCDR is identical to the retrieved VCDR (Fig. 10, left), as theoretically expected, since the calculated difference between the two using the VCDR as reference is less than 0.0007. The PLDR values (Fig. 10, right) of the suspended slightly depolarising particles are in the order of  $0.02 \pm 0.0012$  below 2 km and in the order of  $0.028 \pm 0.0058$  at 2.6 km, while the PCDR values in the same altitude ranges are in the order of  $0.041 \pm 0.0027$  and  $0.059 \pm 0.0014$ , respectively. In all altitude ranges the differences between the PCDR the converted PLDR-to-PCDR using the PCDR as reference are less than 0.018 and inside the statistical uncertainty of the retrieval.



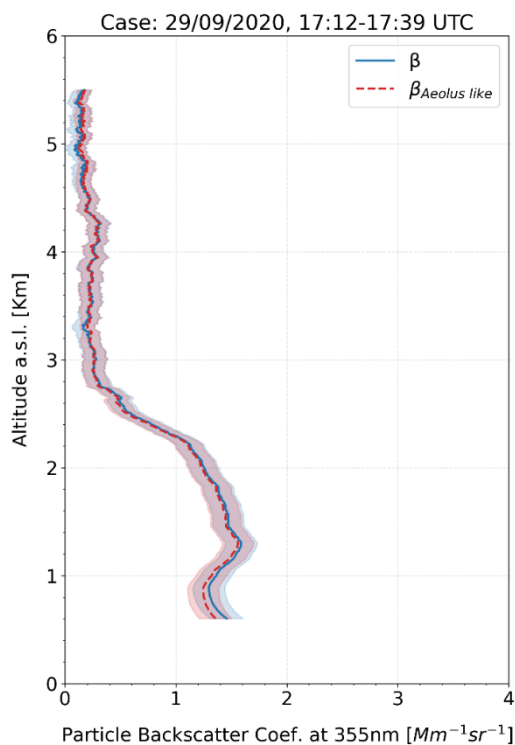
510 **Figure 10: Profiles of the volume depolarisation ratios (left) and the particle depolarisation ratios (right) at 355 nm for the timeframe 17:12 to 17:39 UTC on 29 September 2020. The VLDR and PLDR profiles are presented in blue solid lines, the VCDR and PCDR profiles are presented in orange dashed lines, while the VLDR-to-VCDR and PLDR-to-PCDR profiles are presented in green dotted lines. Shaded regions denote statistical  $1 \sigma$  uncertainty.**

According to the profiles of the particle backscatter coefficient (Fig. 11) and the particle extinction coefficient (Fig. 12) the suspended particles form a thin layer that extends up to 2.6 km with backscatter coefficient values up to  $1.6 \pm 0.14 \text{ Mm}^{-1}\text{sr}^{-1}$  and extinction coefficient mean value of  $17 \pm 1.04 \text{ Mm}^{-1}$ . Due to the absence of strongly depolarising particles in the

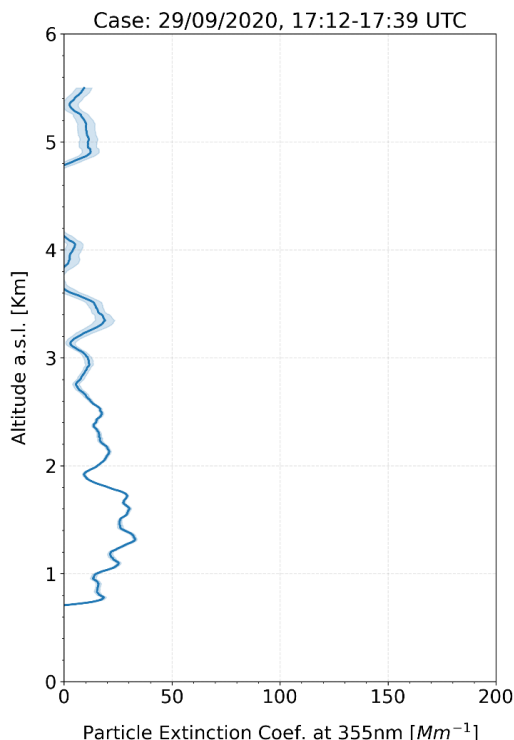
515



atmospheric scene, a very good agreement in all altitude ranges with discrepancies less than  $0.04 \text{ Mm}^{-1}\text{sr}^{-1}$ , which are inside the statistical uncertainty of the retrieval, can be observed between the profiles of the ‘Aeolus like’ backscatter coefficient and the backscatter coefficient in Fig. 11, denoting the expected good performance of Aeolus L2A products under scenes with negligible or no depolarisation.



520 **Figure 11:** The ‘Aeolus like’ particle backscatter coefficient ( $\beta_{Aeolus\ like}$ ; dashed red line) and the particle backscatter coefficient ( $\beta$ ; solid blue line) both retrieved from the circularly polarised signals of eVe lidar on 29 September 2020, from 17:12 to 17:39 UTC. The backscatter coefficient was retrieved using the Raman inversion method and the reference height for Rayleigh atmosphere was selected at 10.3 km with a 0.3 km window. Shaded regions denote statistical  $1\sigma$  uncertainty.



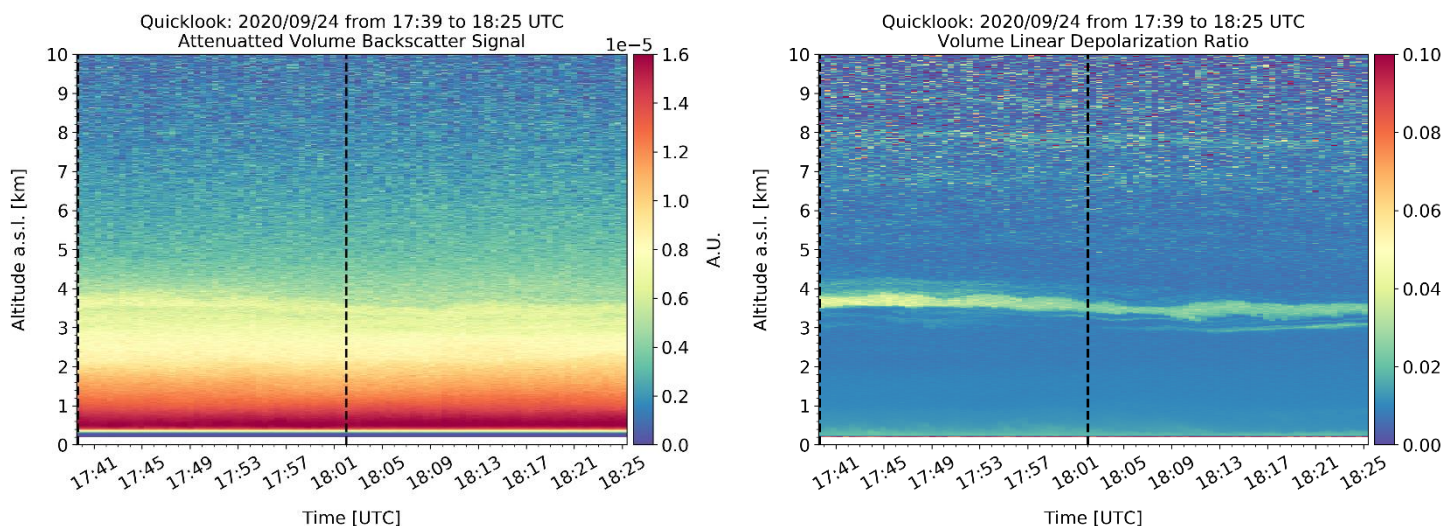
525 **Figure 12:** The profile of the particle extinction coefficient at 355 nm retrieved from eVe lidar on 29 September 2020 from 17:12 to 17:39 UTC. Shaded regions denote statistical  $1\sigma$  uncertainty.

## 5.2. Case study of 24 September 2020

On 24 September 2020, from 17:39 to 18:29 UTC a layer with depolarising particles is present at approximately 4 km over Athens, as shown in the attenuated volume backscatter signal and VLDR profiles in Fig. 13. Above this layer, an aerosol free region is observed up to 7 km. Depolarising layers are also detected between 7 and 8 km, which are not investigated further.

530 From 18:02 UTC to 18:25 UTC, a minor depolarising layer was present at 3 km, just below the mid-altitude layer. To avoid the retrieved optical products to be affected from this minor layer at 3 km and also aiming for homogeneous atmospheric conditions, the timeframe between 17:39 and 18:02 UTC (enclosed by the black dashed lines in Fig. 13) was selected for the retrieval.





535 **Figure 13: Height versus time plots of the attenuated volume backscatter signal from linear emission and the volume linear depolarisation ratio at 355 nm over Athens, measured by eVe lidar on 24 September 2020 from 17:39 to 18:25 UTC. The raw temporal and vertical resolution are 30 s and 3.75 m, respectively, with vertical pointing of the system. The attenuated volume backscatter signal was calibrated using a calibration factor averaged inside the selected timeframe and calculated at 9.8 km within a 0.2 km window. The two back dashed lines enclose the selected timeframe for the optical products retrieval.**

The retrievals inside the selected timeframe of the volume and particle depolarisation ratios are shown in Fig. 14, where the  
540 depolarising layer extends from 3.4 to 3.9 km with mean VLDR and VCDR values of  $0.025 \pm 0.0001$  and  $0.052 \pm 0.0003$ , respectively, and PLDR and PCDR values up to  $0.07 \pm 0.0026$  and  $0.16 \pm 0.0061$ , respectively, indicating a layer with moderately depolarising particles. An optically thinner layer with mean VLDR and VCDR values of  $0.011 \pm 0.0000$  and  $0.022 \pm 0.0000$ , respectively, and mean PLDR and PCDR values of  $0.029 \pm 0.0012$  and  $0.056 \pm 0.0022$ , respectively, is observed in  
545 the lower altitude ranges which gradually decreases with increasing of the altitude. At approximately 5.3 km an optically thinner layer is observed as well, with mean VLDR and VCDR values of  $0.009 \pm 0.0008$  and  $0.018 \pm 0.0003$ , respectively. The corresponding PLDR and PCDR values are in the order of  $0.086 \pm 0.0394$  and  $0.233 \pm 0.125$ , respectively.

In the depolarising layer within the height range between 3.4 and 3.9 km, where the aerosol load increases, a deviation of 0.002 is observed between the retrieved VCDR and the converted VLDR-to-VCDR which is calculated from theory. The same applies also for the particle circular depolarisation ratio, where a deviation of 0.009 is observed between the retrieved PCDR  
550 and the converted PLDR-to-PCDR. These differences indicate deviation of the measurements from the theoretical relationship that connects the linear and circular depolarisation ratio. This deviation can hold when the particles are oriented and/or when multiple scattering is significant. However, this assumption should be further investigated using more measurements over a wide variety of aerosol types and burdens in the atmosphere. In addition, the converted PLDR-to-PCDR deviates from the retrieved PCDR by 0.07 above 5 km. Even though the discrepancy of 0.07 is considerably large, the statistical uncertainty of  
555 retrieval in these altitude ranges (Fig. 14) is too high with values up to 0.16.

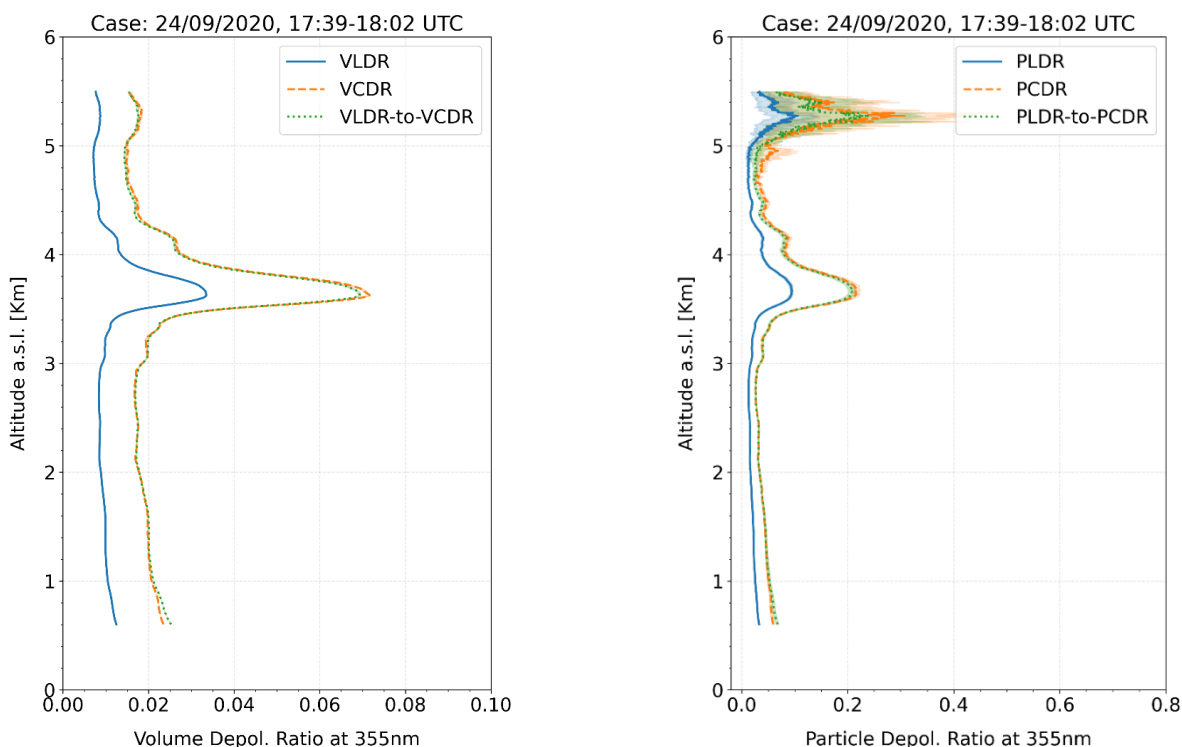
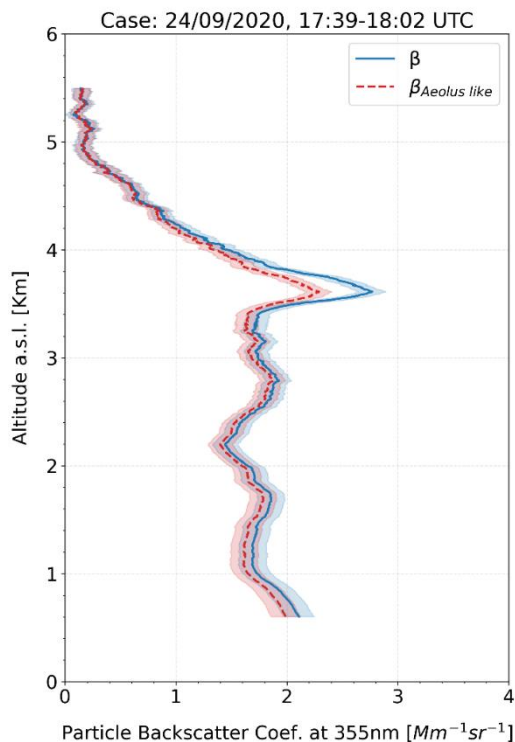


**Figure 14: Profiles of the volume depolarisation ratios (left) and the particle depolarisation ratios (right) at 355 nm for the timeframe 17:39 to 18:02 UTC on 24 September 2020. The VLDR and PLDR profiles are presented in blue solid lines, the VCDR and PCDR profiles are presented in orange dashed lines, while the VLDR-to-VCDR and PLDR-to-PCDR profiles are presented in green dotted lines. Shaded regions denote statistical  $1 \sigma$  uncertainty.**

560 For this case, the particles inside the depolarising layer located from 3.4 to 3.9 km have backscatter values in the order of  $2.8 \pm 0.12 \text{ Mm}^{-1}\text{sr}^{-1}$  according to the particle backscatter coefficient profile in Fig. 15 and mean particle extinction coefficient of  $74 \pm 3.39 \text{ Mm}^{-1}$  (Fig. 16). Below the base of the depolarising layer at 3.4 km, aerosols are also suspended in the atmosphere since the backscatter values range from 1.4 to  $1.9 \text{ Mm}^{-1}\text{sr}^{-1}$  and the extinction values range from 59 to  $82 \text{ Mm}^{-1}$ . Moreover, the ‘Aeolus like’ backscatter coefficient in Fig. 15 is slightly underestimated by approximately 17 % with respect to the backscatter

565 coefficient under the presence of the depolarising particles inside the detected layer at about 3.7 km. An even slighter underestimation of the ‘Aeolus like’ backscatter coefficient, in the order of 5 %, is detected below 2 km, but the corresponding deviations fall within the calculated statistical uncertainty of the retrieval.



570 **Figure 15:** The ‘Aeolus like’ particle backscatter coefficient ( $\beta_{Aeolus\ like}$ ; dashed red line) and the particle backscatter coefficient ( $\beta$ ; solid blue line) both retrieved from the circularly polarised signals of eVe lidar on 24 September 2020, from 17:39 to 18:02 UTC. The backscatter coefficient was retrieved using the Raman inversion method and the reference height for Rayleigh atmosphere was selected at 9.8 km within a 0.2 km window. Shaded regions denote statistical  $1\sigma$  uncertainty.

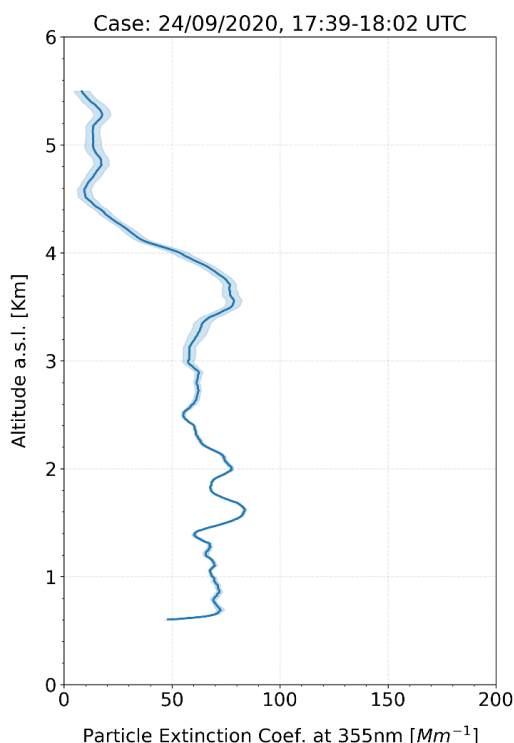


**Figure 16:** The profile of the particle extinction coefficient at 355 nm retrieved from eVe lidar on 24 September 2020 from 17:39 to 18:02 UTC. Shaded regions denote statistical  $1\sigma$  uncertainty.

## 6. Summary and Conclusions

575 eVe lidar is a combined linear/circular polarisation system with Raman capabilities operating at 355 nm. The lidar is specially designed to provide ground-based reference measurements for Cal/Val studies on Aeolus L2A products. The system is also ideal for future EarthCARE Cal/Val activities, due to its linear polarisation measurements and its mobility that allows positioning on the satellite track, a condition that is mandatory for the Cal/Val of spaceborne lidars due to their small footprint. In this paper we described the hardware of the system as well as the developed algorithm for retrieving the optical products of

580 eVe along with two selected cases among the first conducted measurements in Athens. In the first case we examined slightly depolarising particles that are present in the atmosphere with VLDR and VCDR values up to  $0.011 \pm 0.000$  and  $0.022 \pm 0.000$ , respectively, and corresponding PLDR and PCDR values of  $0.028 \pm 0.0058$  and  $0.059 \pm 0.0014$ . In addition, the converted VLDR-to-VCDR and the PLDR-to-PCDR profiles present a very good agreement with respect to the retrieved VCDR and PCDR profiles, respectively. The same applies also between the profiles of the particle backscatter coefficient and the Aeolus

585 like backscatter coefficient, as expected in such atmospheric conditions. In the second case, the suspended particles are moderately depolarising with VLDR and VCDR values of  $0.025 \pm 0.0001$  and  $0.052 \pm 0.0003$ , respectively, and corresponding PLDR and PCDR values of  $0.07 \pm 0.0026$  and  $0.16 \pm 0.0061$ , respectively. Inside the depolarising layer where the AOD is



increased with respect to the rest profile, the converted volume and particle circular depolarisation ratios (VLDR-to-VCDR and PLDR-to-PCDR) deviate from the retrieved ones (VCDR and PCDR) by 0.002 and 0.009, respectively. In addition, an  
590 underestimation of 17% is observed for the Aeolus like backscatter coefficient with respect to the measured particle backscatter coefficient.

Besides eVe's main goal of providing reference measurements for Cal/Val studies on ESA's satellite missions, an interesting application of eVe lidar is related to the possible differences between circular and linear polarisation, arisen most probably by multiple scattering and particle orientation effects. This effect could possibly increase due to the AOD and for non-spherical  
595 particles (Mishchenko and Hovenier, 1995; Roy and Roy, 2008), as is slightly indicated by the two case studies presented in this work. Multiple scattering effects in dust layers have only been detected from instruments onboard satellite platforms like CALIPSO (Wandinger et al., 2010; Yoshida et al., 2010). On the other hand, regarding the randomly oriented particles assumption, it has recently reported theoretically in Mallios et al., (2021) and experimentally in Daskalopoulou et al., (2021), that the dust particles can have a preferential vertical plane of orientation. Thus, the particle orientation seems to be a reasonable  
600 explanation for the observed deviations between the converted and retrieved circular depolarisation ratios in case of desert dust. Nevertheless, the validity of the theoretical relationship between linear and circular depolarisation ratio has to be further investigated by performing more measurements in dust layers, cirrus clouds and/or scenes when different aerosol types are probed, before a definite explanation is given. An added value in this kind of studies will be the collocated measurements with the polarisation lidar of NOAA, nicknamed "WALL-E" (Tsekeri et al., 2021) which is specifically designed to detect and  
605 characterize dust particle orientation. In addition, the concept of dual FOV technique (Jimenez et al., 2020b) can be implemented in the system in order to attempt extracting information about the multiple scattering contribution on dust layers. These aspects will be examined in the future using eVe measurements that are collected during the experimental campaigns that have been scheduled by ESA, e.g., the ASKOS experiment under the Joint Aeolus – Tropical Atlantic Campaign 2021 (JATAC) on the islands of Cape Vere.

## 610 **Appendix A. Harmonization of polarisation lidar systems with Aeolus L2A products**

### **A1. Theoretical background**

The laser beam emitted from a lidar system interacts with the atmospheric constituents and part of it is scattered at the backward direction. The total backscattered light is quantified using the backscatter coefficient ( $\beta$ ), defined in cloud-free atmospheres as the sum of the particle (i.e., aerosol) backscatter coefficient ( $\beta^p$ ) and the molecular backscatter coefficient ( $\beta^m$ ).

$$\beta = \beta^p + \beta^m \quad (\text{A1})$$

615 The lidar ratio ( $L$ ) is defined as the ratio of the extinction to backscatter coefficients. The particle backscatter-to-extinction ratio ( $BER$ ) is the inverted particle lidar ratio  $L^p$ .

$$L^p = \frac{\alpha^p}{\beta^p} = \frac{1}{BER} \quad (\text{A2})$$



In a lidar setup the measured total signal from the collected backscattered light is described from the following equation:

$$I(z) = \frac{A_0}{z^2} C \beta(z) T^2(z) \quad (\text{A3})$$

where  $A_0$  is the system constant,  $C$  is the calibration factor, and  $T^2(z)$  is the atmospheric transmittance from the lidar to the scattering volume and back.

620 In polarisation sensitive lidar systems the backscattered light from linearly or circularly polarised emission is optically separated with a polarisation analyser in two components and thus two signals can be measured. The parallel or co-polar component ( $\parallel$ ) contains the backscattered light with the original polarisation and half of the depolarised light whereas the cross or cross-polar component ( $\perp$ ) contains the other half of the depolarised light (Gimmestad, 2008). According to Gimmestad, (2008), in case of randomly oriented particles in the atmosphere and for single-scattered light backwards the lidar equations  
 625 of the two measured signal components can be written as:

$$I_{\parallel}(z) = \frac{A_0}{z^2} C_{\parallel} f_{\parallel}(a) \beta(z) \exp(-2 \int_0^z \alpha(r) dr) \quad (\text{A4})$$

and

$$I_{\perp}(z) = \frac{A_0}{z^2} C_{\perp} f_{\perp}(a) \beta(z) \exp(-2 \int_0^z \alpha(r) dr) \quad (\text{A5})$$

In the lidar equations (A4) and (A5) the measured signals depend on a function of the atmospheric depolarisation parameter  $d$  (Gimmestad, 2008) or the polarisation parameter ( $a = 1 - d$ ; (Freudenthaler, 2016)). The function describes the result of the interaction of the emitted polarised light with the atmosphere and the optical elements of the lidar. For linearly polarised  
 630 emission and a linear polarisation analyser in the lidar receiver the functions in the measured signal components are:

$$f_{\parallel,lin}(a) = \frac{1+a}{2} \quad (\text{A6})$$

$$f_{\perp,lin}(a) = \frac{1-a}{2} \quad (\text{A7})$$

While, for circularly polarised emission and circular polarisation analyser in the lidar setup the functions are modified as:

$$f_{\parallel,cir}(a) = a \quad (\text{A8})$$

$$f_{\perp,cir}(a) = 1 - a \quad (\text{A9})$$

The total backscatter coefficient for different scatterer types  $i$  ( $p$  for particles,  $m$  for molecules,  $v$  for volume) and for emitted light of linear or circular polarisation ( $j = lin, cir$ ) can be written as:

$$\beta^i = f_{\parallel,j}(a^i) \beta^i + f_{\perp,j}(a^i) \beta^i \quad (\text{A10})$$

Mishchenko and Hovenier, (1995) define the depolarisation ratio ( $\delta$ ) as the ratio of the cross or cross-polar to the parallel or  
 635 co-polar measured signal components depending on the polarisation state of the emission (linear or circular). The signal ratio is corrected with the polarisation calibration factor ( $\eta = C_{\perp}/C_{\parallel}$ ) which includes their relative amplification differences (Freudenthaler, 2016). Hence, the depolarisation ratio that holds for linear and circular polarisation can be derived using the polarisation parameter  $a$ .

$$\delta = \frac{1}{\eta} \frac{I_{\perp}}{I_{\parallel}} = \frac{f_{\perp}(a)}{f_{\parallel}(a)} \quad (\text{A11})$$



Depending on the scatterer type  $i$  ( $i = v, p, m$ ), the linear depolarisation ratio ( $\delta_{lin}^i$ ) is obtained from Eq. (A12) while the  
 640 circular depolarisation ratio ( $\delta_{cir}^i$ ) is obtained from Eq. (A13).

$$\delta_{lin}^i = \frac{1-a^i}{1+a^i} \quad (\text{A12})$$

$$\delta_{cir}^i = \frac{1-a^i}{a^i} \quad (\text{A13})$$

Equation (A14) is derived using equations (A12) and (A13), and provides the formula between the linear depolarisation ratio  
 ( $\delta_{lin}^i$ ) and the circular depolarisation ratio ( $\delta_{cir}^i$ ), in case of randomly oriented particles in the atmosphere and under single  
 scattering assumption (Mishchenko and Hovenier, 1995; Roy and Roy, 2008):

$$\delta_{cir}^i = \frac{2\delta_{lin}^i}{1-\delta_{lin}^i} \quad (\text{A14})$$

## A2. How to convert the polarisation lidar products to Aeolus L2A optical products

645 Since ALADIN onboard Aeolus detects only the co-polar component of the backscattered circularly polarised light, the lidar  
 equation that describes the detected signal is eq. (A4). Consequently, Aeolus retrieves the quantity  $f_{\parallel, cir}(a^p)\beta^p$  named as co-  
 polar backscatter coefficient. The co-polar backscatter coefficient does not have a physical meaning (Gimmestad, 2008) and  
 it is used only to name the quantity that is retrieved from Aeolus as the L2A product of particle backscatter coefficient.  
 The ground-based polarisation lidars can use their measurements of the particle backscatter coefficient, the lidar ratio, and the  
 650 volume and particle depolarisation ratios to derive products that are comparable with the Aeolus L2A products with the  
 following steps:

1. The particle linear depolarisation ratio ( $\delta_{lin}^p$ ) retrieved from ground-based polarisation lidar with linearly polarised  
 emission can be converted to the particle circular depolarisation ratio ( $\delta_{cir}^p$ ) using Eq. (A14).
2. The particle backscatter coefficient ( $\beta^p$ ) is converted to the ‘Aeolus like’ backscatter coefficient ( $\beta_{Aeolus\ like}$ ) using  
 655 the equations (A10) and (A11):

$$\beta_{Aeolus\ like} = f_{\parallel, cir}(a^p)\beta^p = \frac{\beta^p}{1+\delta_{cir}^p} \quad (\text{A15})$$

3. The ‘Aeolus like’ particle BER is calculated using the ‘Aeolus like’ backscatter coefficient from Eq. (A15):

$$BER = \frac{\beta_{Aeolus\ like}}{\alpha^p} \quad (\text{A16})$$

Thus, the ‘Aeolus like’ lidar ratio ( $L_{Aeolus\ like}$ ) is derived using  $L^p$  and  $\delta_{cir}^p$ :

$$L_{Aeolus\ like} = \frac{\alpha^p}{\beta_{Aeolus\ like}^p} = \frac{\alpha^p(1+\delta_{cir}^p)}{\beta^p} = L^p(1 + \delta_{cir}^p) \quad (\text{A17})$$



### Author contribution

660 PP and NS tested and optimized the instrument, and acquired the measurements shown herein with the support of AL, GG, AT, GT, CE and VF. PP and NS developed the software for processing the measurements and performing quality assurance tests, and retrieving the optical products. NS and VF formulated the measurement strategy and the emission and detection design of the system, along with the calibration procedures. VF conceived the "dual-laser/dual-telescope" concept, and GG and AL developed the optomechanical design of the instrument. PP made the analysis of the acquired measurements and the manuscript preparation with the support of NS. VF, AT, VA, IB, and JvB provided corrections and suggestions. VA supervised and directed the whole project. All authors provided critical feedback and helped shape the research, analysis and manuscript.

665

### Competing interests

The authors declare that they have no conflict of interest.

### Special issue statement

670 This article is part of the special issue "Aeolus data and their application" and it does not belong to a conference.

### Acknowledgements

The authors acknowledge the support of the project "PANhellenic infrastructure for Atmospheric Composition and climate change" (MIS 5021516), implemented under the Action "Reinforcement of the Research and Innovation Infrastructure", funded by the Operational Programme "Competitiveness, Entrepreneurship and Innovation" (NSRF 2014-2020) and co-financed by Greece and the European Union (Euro-pean Regional Development Fund); the European Research Council under the European Community's Horizon 2020 research and innovation frame-work program/ERC Grant Agreement 725698 (D-TECT), and the Stavros Niarchos Foundation. The lidar system was developed by Raymetrics S.A. under an ESA project (contract No. 4000127438/19/I-BG) in collaboration with the National Observatory of Athens and the Ludwig-Maximilians-Universität.

675

### 680 References

Ansmann, A., Wandinger, U., Riebesell, M., Weitkamp, C. and Michaelis, W.: Independent measurement of extinction and backscatter profiles in cirrus clouds by using a combined Raman elastic-backscatter lidar, *Appl. Opt.*, 31(33), 7113–7131, doi:10.1364/AO.31.007113, 1992.

Ansmann, A., Wandinger, U., Le Rille, O., Lajas, D. and Straume, A. G.: Particle backscatter and extinction profiling with the





- 685 spaceborne high-spectral-resolution Doppler lidar ALADIN: methodology and simulations, *Appl. Opt.*, 46(26), 6606, doi:10.1364/AO.46.006606, 2007.
- Ansmann, A., Tesche, M., Groß, S., Freudenthaler, V., Seifert, P., Hiebsch, A., Schmidt, J., Wandinger, U., Mattis, I., Müller, D. and Wiegner, M.: The 16 April 2010 major volcanic ash plume over central Europe: EARLINET lidar and AERONET photometer observations at Leipzig and Munich, Germany, *Geophys. Res. Lett.*, 37(13), doi:10.1029/2010GL043809, 2010.
- 690 Belegante, L., Bravo-Aranda, J. A., Freudenthaler, V., Nicolae, D., Nemuc, A., Ene, D., Alados-Arboledas, L., Amodeo, A., Pappalardo, G., D'Amico, G., Amato, F., Engelmann, R., Baars, H., Wandinger, U., Papayannis, A., Kokkalis, P. and Pereira, S. N.: Experimental techniques for the calibration of lidar depolarization channels in EARLINET, *Atmos. Meas. Tech.*, 11(2), 1119–1141, doi:10.5194/amt-11-1119-2018, 2018.
- Beyerle, G.: Untersuchungen stratosphärischer Aerosole vulkanischen Ursprungs und polarer stratosphärischer Wolken mit einem Mehrwellen-Lidar auf Spitzbergen (79°N, 12°E) = Multiwavelength lidar measurements of stratospheric volcanic aerosols and polar stratospheric c, *Berichte zur Polarforsch. (Reports Polar Res.)*, 138, doi:10.2312/BzP\_0138\_1994, 1994.
- 695 Böckmann, C., Wandinger, U., Ansmann, A., Bösenberg, J., Amiridis, V., Boselli, A., Delaval, A., Tomasi, F. De, Frioud, M., Grigorov, I. V., Hågård, A., Horvat, M., Iarlori, M., Komguem, L., Kreipl, S., Larchevêque, G., Matthias, V., Papayannis, A., Pappalardo, G., Rocadenbosch, F., Rodrigues, J. A., Schneider, J., Shcherbakov, V. and Wiegner, M.: Aerosol lidar intercomparison in the framework of the EARLINET project. 2. Aerosol backscatter algorithms, *Appl. Opt.*, 43(4), 977–989, doi:10.1364/AO.43.000977, 2004.
- 700 Chipman, R. A.: Mueller matrices, in *Handbook of Optics: Volume I - Geometrical and Physical Optics, Polarized Light, Components and Instruments*, Third Edition, edited by M. Bass, McGraw-Hill Professional., 2009a.
- Chipman, R. A.: Polarimetry, in *Handbook of Optics: Volume I - Geometrical and Physical Optics, Polarized Light, Components and Instruments*, Third Edition, edited by M. Bass, McGraw-Hill Professional., 2009b.
- 705 D'Amico, G., Amodeo, A., Mattis, I., Freudenthaler, V. and Pappalardo, G.: EARLINET Single Calculus Chain --technical - - Part 1: Pre-processing of raw lidar data, *Atmos. Meas. Tech.*, doi:10.5194/amt-9-491-2016, 2016.
- Dabas, A.: Observing the atmospheric wind from space, *Comptes Rendus Geosci.*, 342(4–5), 370–379, doi:10.1016/J.CRTE.2009.09.014, 2010.
- 710 Daskalopoulou, V., Raptis, P. I., Tsekeri, A., Amiridis, V., Kazadzis, S., Ulanowski, Z., Metallinos, S., Tassis, K. and Wirth, M.: Monitoring dust particle orientation with measurements of sunlight dichroic extinction, in *15th COMECAP.*, 2021.
- Donovan, D. P., Whiteway, J. A. and Carswell, A. I.: Correction for nonlinear photon-counting effects in lidar systems, *Appl. Opt.*, 32(33), 6742, doi:10.1364/AO.32.006742, 1993.
- Donovan, D. P., Klein Baltink, H., Henzing, J. S., de Roode, S. R. and Siebesma, A. P.: A depolarisation lidar-based method for the determination of liquid-cloud microphysical properties, *Atmos. Meas. Tech.*, 8(1), 237–266, doi:10.5194/amt-8-237-2015, 2015.
- 715 Engelmann, R., Kanitz, T., Baars, H., Heese, B., Althausen, D., Skupin, A., Wandinger, U., Komppula, M., Stachlewska, I. S., Amiridis, V., Marinou, E., Mattis, I., Linné, H. and Ansmann, A.: The automated multiwavelength Raman polarization and



- water-vapor lidar PollyXT: The neXT generation, *Atmos. Meas. Tech.*, doi:10.5194/amt-9-1767-2016, 2016.
- 720 Evans, R. D.: The atomic nucleus, McGraw-Hill, New York., 1955.
- Fernald, F. G.: Analysis of atmospheric lidar observations: some comments, *Appl. Opt.*, 23(5), 652–653, doi:10.1364/AO.23.000652, 1984.
- Flamant, P., Lever, V., Martinet, P., Flament, T., Cuesta, J., Dabas, A., M., O. and Huber, D.: AE-TN-IPSL-GS-001 v5.5: ADM-Aeolus L2A Algorithm Theoretical Baseline Document. [online] Available from:  
725 [https://earth.esa.int/pi/esa?type=file&table=aotarget&cmd=image&alias=Aeolus\\_L2A\\_Algorithm\\_TBD](https://earth.esa.int/pi/esa?type=file&table=aotarget&cmd=image&alias=Aeolus_L2A_Algorithm_TBD), 2007.
- Flamant, P., Cuesta, J., Denneulin, M.-L., Dabas, A. and Huber, D.: ADM-Aeolus retrieval algorithms for aerosol and cloud products, *Tellus A*, 60(2), 273–288, doi:10.1111/j.1600-0870.2007.00287.x, 2008.
- Freudenthaler, V.: Effects of spatially inhomogeneous photomultiplier sensitivity on lidar signals and remedies, in 22nd International Laser Radar Conference (ILRC 2004), vol. 561, p. 37., 2004.
- 730 Freudenthaler, V.: About the effects of polarising optics on lidar signals and the  $\Delta 90$  calibration, *Atmos. Meas. Tech.*, 9(9), 4181–4255, doi:10.5194/amt-9-4181-2016, 2016.
- Freudenthaler, V., Esselborn, M., Wiegner, M., Heese, B., Tesche, M., Ansmann, A., Müller, D., Althausen, D., Wirth, M., Fix, andreas, Ehret, G., Knippertz, P., Toledano, C., Gasteiger, J., Garhammer, M. and Seefeldner, M.: Depolarization ratio profiling at several wavelengths in pure Saharan dust during SAMUM 2006, *Tellus B*, 61(1), 165–179, doi:10.1111/j.1600-  
735 0889.2008.00396.x, 2009.
- Freudenthaler, V., Linné, H., Chaikovski, A., Rabus, D. and Groß, S.: EARLINET lidar quality assurance tools, *Atmos. Meas. Tech. Discuss.*, 1–35, doi:10.5194/amt-2017-395, 2018.
- Gialitaki, A., Tsekeri, A., Amiridis, V., Ceolato, R., Paulien, L., Kampouri, A., Gkikas, A., Solomos, S., Marinou, E., Haarig, M., Baars, H., Ansmann, A., Lapyonok, T., Lopatin, A., Dubovik, O., Groß, S., Wirth, M., Tschla, M., Tsikoudi, I. and Balis,  
740 D.: Is the near-spherical shape the “new black” for smoke?, *Atmos. Chem. Phys.*, 20(22), doi:10.5194/acp-20-14005-2020, 2020.
- Gimmestad, G. G.: Reexamination of depolarization in lidar measurements, *Appl. Opt.*, 47(21), 3795, doi:10.1364/AO.47.003795, 2008.
- Holben, B. N., Eck, T. F., Slutsker, I., Tanré, D., Buis, J. P., Setzer, A., Vermote, E., Reagan, J. A., Kaufman, Y. J., Nakajima,  
745 T., Lavenu, F., Jankowiak, I. and Smirnov, A.: AERONET - A federated instrument network and data archive for aerosol characterization, *Remote Sens. Environ.*, doi:10.1016/S0034-4257(98)00031-5, 1998.
- van de Hulst, H. C.: Light scattering by small particles., Wiley, New York., 1957.
- Illingworth, A. J., Barker, H. W., Beljaars, A., Ceccaldi, M., Chepfer, H., Clerbaux, N., Cole, J., Delanoë, J., Domenech, C., Donovan, D. P., Fukuda, S., Hirakata, M., Hogan, R. J., Huenerbein, A., Kollias, P., Kubota, T., Nakajima, T., Nakajima, T.,  
750 Y., Nishizawa, T., Ohno, Y., Okamoto, H., Oki, R., Sato, K., Satoh, M., Shephard, M. W., Velázquez-Blázquez, A., Wandinger, U., Wehr, T. and Van Zadelhoff, G. J.: The earthcare satellite : The next step forward in global measurements of clouds, aerosols, precipitation, and radiation, *Bull. Am. Meteorol. Soc.*, doi:10.1175/BAMS-D-12-00227.1, 2015.



- Imaki, M., Takegoshi, Y. and Kobayashi, T.: Ultraviolet High-Spectral-Resolution Lidar with Fabry–Perot Filter for Accurate Measurement of Extinction and Lidar Ratio, *Jpn. J. Appl. Phys.*, 44(5A), 3063–3067, doi:10.1143/JJAP.44.3063, 2005.
- 755 Jimenez, C., Ansmann, A., Engelmann, R., Donovan, D., Malinka, A., Seifert, P., Wiesen, R., Radenz, M., Yin, Z., Bühl, J., Schmidt, J., Barja, B. and Wandinger, U.: The dual-field-of-view polarization lidar technique: a new concept in monitoring aerosol effects in liquid-water clouds – case studies, *Atmos. Chem. Phys.*, 20(23), 15265–15284, doi:10.5194/acp-20-15265-2020, 2020a.
- Jimenez, C., Ansmann, A., Engelmann, R., Donovan, D., Malinka, A., Schmidt, J., Seifert, P. and Wandinger, U.: The dual-  
760 field-of-view polarization lidar technique: a new concept in monitoring aerosol effects in liquid-water clouds – theoretical framework, *Atmos. Chem. Phys.*, 20(23), 15247–15263, doi:10.5194/acp-20-15247-2020, 2020b.
- Klett, J. D.: Stable analytical inversion solution for processing lidar returns, *Appl. Opt.*, 20(2), 211–220, doi:10.1364/AO.20.000211, 1981.
- Licel GmbH: TR40-16bit-3U Lidar transient recorder, Berlin, Germany. [online] Available from:  
765 [http://licel.com/manuals/TR40-16bit3U\\_Manual.pdf](http://licel.com/manuals/TR40-16bit3U_Manual.pdf), 2020.
- Lolli, S., Delaval, A., Loth, C., Garnier, A. and Flamant, P. H.: 0.355-micrometer direct detection wind lidar under testing during a field campaign in consideration of ESA’s ADM-Aeolus mission, *Atmos. Meas. Tech.*, 6(12), 3349–3358, doi:10.5194/amt-6-3349-2013, 2013.
- Lu, S.-Y. and Chipman, R. A.: Interpretation of Mueller matrices based on polar decomposition, *J. Opt. Soc. Am. A*, 13(5),  
770 1106, doi:10.1364/JOSAA.13.001106, 1996.
- Mallios, S. A., Daskalopoulou, V. and Amiridis, V.: Orientation of non spherical prolate dust particles moving vertically in the Earth’s atmosphere, *J. Aerosol Sci.*, 151, 105657, doi:https://doi.org/10.1016/j.jaerosci.2020.105657, 2021.
- Mattis, I., D’Amico, G., Baars, H., Amodeo, A., Madonna, F. and Iarlori, M.: EARLINET Single Calculus Chain – technical – Part 2: Calculation of optical products, *Atmos. Meas. Tech.*, 9(7), 3009–3029, doi:10.5194/amt-9-3009-2016, 2016.
- 775 Mishchenko, M. I. and Hovenier, J. W.: Depolarization of light backscattered by randomly oriented nonspherical particles, *Opt. Lett.*, 20(12), 1356, doi:10.1364/OL.20.001356, 1995.
- Mishchenko, M. I. and Sassen, K.: Depolarization of lidar returns by small ice crystals: An application to contrails, *Geophys. Res. Lett.*, 25(3), 309–312, doi:https://doi.org/10.1029/97GL03764, 1998.
- Mishchenko, M. I., Travis, L. D. and Lacis, A. A.: *Scattering, Absorption and Emission of Light by Small Particles.*, 2002.
- 780 Myagkov, A., Seifert, P., Wandinger, U., Bühl, J. and Engelmann, R.: Relationship between temperature and apparent shape of pristine ice crystals derived from polarimetric cloud radar observations during the ACCEPT campaign, *Atmos. Meas. Tech.*, 9(8), 3739–3754, doi:10.5194/amt-9-3739-2016, 2016.
- Noel, V. and Sassen, K.: Study of planar ice crystal orientations in ice clouds from scanning polarization lidar observations, *J. Appl. Meteorol.*, 44(5), doi:10.1175/JAM2223.1, 2005.
- 785 Paffrath, U., Lemmerz, C., Reitebuch, O., Witschas, B., Nikolaus, I. and Freudenthaler, V.: The Airborne Demonstrator for the Direct-Detection Doppler Wind Lidar ALADIN on ADM-Aeolus. Part II: Simulations and Rayleigh Receiver Radiometric



- Performance, J. *Atmos. Ocean. Technol.*, 26(12), 2516–2530, doi:10.1175/2009JTECHA1314.1, 2009.
- Pappalardo, G., Amodeo, A., Pandolfi, M., Wandinger, U., Ansmann, A., Bösenberg, J., Matthias, V., Amiridis, V., Tomasi, F. De, Frioud, M., Iarlori, M., Komguem, L., Papayannis, A., Rocadenbosch, F. and Wang, X.: Aerosol lidar intercomparison in the framework of the EARLINET project. 3. Ramanlidar algorithm for aerosol extinction, backscatter, and lidar ratio, *Appl. Opt.*, 43(28), 5370–5385, doi:10.1364/AO.43.005370, 2004.
- Pappalardo, G., Amodeo, A., Apituley, A., Comeron, A., Freudenthaler, V., Linné, H., Ansmann, A., Bösenberg, J., D&apos;Amico, G., Mattis, I., Mona, L., Wandinger, U., Amiridis, V., Alados-Arboledas, L., Nicolae, D. and Wiegner, M.: EARLINET: towards an advanced sustainable European aerosol lidar network, *Atmos. Meas. Tech.*, 7(8), 2389–2409, doi:10.5194/amt-7-2389-2014, 2014.
- Reitebuch, O.: The Spaceborne Wind Lidar Mission ADM-Aeolus, edited by U. Schumann, pp. 815–827, Springer Berlin Heidelberg, Berlin, Heidelberg., 2012.
- Reitebuch, O., Lemmerz, C., Nagel, E., Paffrath, U., Durand, Y., Endemann, M., Fabre, F. and Chaloupy, M.: The Airborne Demonstrator for the Direct-Detection Doppler Wind Lidar ALADIN on ADM-Aeolus. Part I: Instrument Design and Comparison to Satellite Instrument, *J. Atmos. Ocean. Technol.*, 26(12), 2501–2515, doi:10.1175/2009JTECHA1309.1, 2009.
- Robert, C. P. and Casella, G.: *Monte Carlo Statistical Methods*, Springer Publishing Company, Incorporated., 2010.
- Roy, G. and Roy, N.: Relation between circular and linear depolarization ratios under multiple-scattering conditions, *Appl. Opt.*, doi:10.1364/ao.47.006563, 2008.
- Sasano, Y. and Nakane, H.: Significance of the extinction/backscatter ratio and the boundary value term in the solution for the two-component lidar equation, *Appl. Opt.*, 23(1), 11\_1--13, doi:10.1364/AO.23.0011\_1, 1984.
- Sassen, K.: Boreal tree pollen sensed by polarization lidar: Depolarizing biogenic chaff, *Geophys. Res. Lett.*, 35(18), doi:https://doi.org/10.1029/2008GL035085, 2008.
- Schmidt, J., Wandinger, U. and Malinka, A.: Dual-field-of-view Raman lidar measurements for the retrieval of cloud microphysical properties, *Appl. Opt.*, 52(11), 2235, doi:10.1364/AO.52.002235, 2013.
- Shiple, S. T., Tracy, D. H., Eloranta, E. W., Trauger, J. T., Sroga, J. T., Roesler, F. L. and Weinman, J. A.: High spectral resolution lidar to measure optical scattering properties of atmospheric aerosols 1: Theory and instrumentation, *Appl. Opt.*, 22(23), 3716, doi:10.1364/AO.22.003716, 1983.
- Simeonov, V., Larcheveque, G., Quaglia, P., van den Bergh, H. and Calpini, B.: Influence of the photomultiplier tube spatial uniformity on lidar signals, *Appl. Opt.*, 38(24), doi:10.1364/ao.38.005186, 1999.
- Stoffelen, A., Pailleux, J., Källén, E., Vaughan, J. M., Isaksen, L., Flamant, P., Wergen, W., Andersson, E., Schyberg, H., Culoma, A., Meynard, R., Endemann, M. and Ingmann, P.: The atmospheric dynamics mission for global wind field measurement, *Bull. Am. Meteorol. Soc.*, 86(1), 73–88, doi:10.1175/BAMS-86-1-73, 2005.
- Stoffelen, A., Marseille, G. J., Bouttier, F., Vasiljevic, D., de Haan, S. and Cardinali, C.: ADM-Aeolus Doppler wind lidar Observing System Simulation Experiment, *Q. J. R. Meteorol. Soc.*, 132(619), 1927–1947, doi:10.1256/qj.05.83, 2006.
- Tan, D. G. H., Andersson, E., Kloe, J. De, Marseille, G.-J., Stoffelen, A., Poli, P., Denneulin, M.-L., Dabas, A., Huber, D.,



- Reitebuch, O., Flamant, P., Rille, O. Le and Nett, H.: The ADM-Aeolus wind retrieval algorithms, *Tellus A Dyn. Meteorol. Oceanogr.*, 60(2), 191–205, doi:10.1111/j.1600-0870.2007.00285.x, 2008.
- Thomas, L., Cartwright, J. C. and Wareing, D. P.: Lidar observations of the horizontal orientation of ice crystals in cirrus clouds, *Tellus, Ser. B*, 42 B(2), doi:10.3402/tellusb.v42i2.15206, 1990.
- 825 Tsekeri, A., Freudenthaler, V., Amiridis, V., Doxastakis, G., Louridas, A., Georgoussis, G., Metallinos, S., Gasteiger, J., Siomos, N., Paschou, P., Georgiou, T., Tsaknakis, G., Evangelatos, C., Biniotoglou, I., Koutroumbas, K. and Rontogiannis, A.: Polarization lidar for detecting dust orientation: System design and calibration, *Atmos. Meas. Tech. Discuss.*, doi:10.5194/amt-2021-30, 2021.
- Ulanowski, Z., Bailey, J., Lucas, P. W., Hough, J. H. and Hirst, E.: Alignment of atmospheric mineral dust due to electric field, *Atmos. Chem. Phys.*, 7(24), 6161–6173, doi:10.5194/acp-7-6161-2007, 2007.
- 830 Wandinger, U. and Ansmann, A.: Experimental determination of the lidar overlap profile with Raman lidar, *Appl. Opt.*, 41(3), 511–514, doi:10.1364/AO.41.000511, 2002.
- Wandinger, U., Tesche, M., Seifert, P., Ansmann, A., Müller, D. and Althausen, D.: Size matters: Influence of multiple scattering on CALIPSO light-extinction profiling in desert dust, *Geophys. Res. Lett.*, 37(10), doi:<https://doi.org/10.1029/2010GL042815>, 2010.
- 835 Weitkamp, C.: *Lidar Range-Resolved Optical Remote Sensing of the Atmosphere*, Springer, New York, NY., 2005.
- Yoshida, R., Okamoto, H., Hagihara, Y. and Ishimoto, H.: Global analysis of cloud phase and ice crystal orientation from Cloud-Aerosol Lidar and Infrared Pathfinder Satellite Observation (CALIPSO) data using attenuated backscattering and depolarization ratio, *J. Geophys. Res. Atmos.*, 115(16), doi:10.1029/2009JD012334, 2010.

840